

# Accelerated boundary integral method for multiphase flow in non-periodic geometries

Amit Kumar, Michael D. Graham\*

*Department of Chemical and Biological Engineering, University of Wisconsin-Madison, Madison, Wisconsin 53706, USA*

---

## Abstract

An accelerated boundary integral method for Stokes flow of a suspension of deformable particles is presented for an arbitrary domain and implemented for the important case of a planar slit geometry. The computational complexity of the algorithm scales as  $O(N)$  or  $O(N \log N)$ , where  $N$  is proportional to the product of number of particles and the number of elements employed to discretize the particle. This technique is enabled by the use of an alternative boundary integral formulation in which the velocity field is expressed in terms of a single layer integral alone, even in problems with non-matched viscosities. The density of the single layer integral is obtained from a Fredholm integral equation of the second kind involving the double layer integral. Acceleration in this implementation is provided by the use of General Geometry Ewald-like method (GGEM) for computing the velocity and stress fields driven by a set of point forces in the geometry of interest. For the particular case of the slit geometry, a Fourier-Chebyshev spectral discretization of GGEM is developed. Efficient implementations employing the GGEM methodology are presented for the resulting single and the double layer integrals. The implementation is validated with test problems on the velocity of rigid particles and drops between parallel walls in pressure driven flow, the Taylor deformation parameter of capsules in simple shear flow and the particle trajectory in pair collisions of capsules in simple shear flow. The computational complexity of the algorithm is verified with results from several large scale multiparticle simulations.

*Keywords:* accelerated boundary integral, confined, slit, non-periodic, capsule, red blood cells, microfluidics

---

## 1. Introduction

Multiphase flow in confined geometries is ubiquitous in nature and technological applications. A very common example is blood flow in the microcirculation. Recall that blood is primarily a suspension of red blood cells (RBCs) in plasma, with the volume fraction  $\phi$  of RBCs (hematocrit) typically ranging between

---

\*Corresponding author

*Email address:* graham@engr.wisc.edu (Michael D. Graham )

$\phi \sim 0.1 - 0.3$  in the capillaries and reaching as high as  $\phi \approx 0.5$  in large arteries [17]. The diameter of the blood vessels in the microcirculation, which includes the capillaries, arterioles and venules, is typically in the range  $10 - 125 \mu m$  [17], such that a discoidal RBC with a typical diameter and thickness of  $8 \mu m$  and  $2 \mu m$  respectively can be strongly to moderately confined. Therefore, any realistic computational study of blood flow in the capillaries must account for confinement. Other examples of technological interest where confinement effects are usually significant include multiphase flows in microfluidic devices [59]. Again, any realistic model must account for confinement in such problems. Given the importance of multiphase flows under confinement, or more generally speaking in non-periodic geometries, it is imperative to develop efficient and accurate computational techniques which faithfully represent the system under study, including the aspect of system size (meaning number of particles here). The algorithm presented herein has been motivated by our goal to study the class of problems described above. We next discuss some related previous efforts on the computational studies of multiphase flows under confinement.

Boundary integral based methods have emerged as a powerful tool for studying the flow behavior of multiphase systems in the limit of negligible Reynolds number, i.e. under Stokes flow conditions. Such methods have been employed in the past to study the flow behavior of a variety of particle types including drops, capsules, RBCs, and vesicles among others. Most of these prior implementations scale as  $O(N^2)$ , where  $N$  is proportional to the number of degrees of freedom in the system. For a system with  $N_p$  particles, each of which have been discretized into  $N_\Delta$  elements, the number of degrees of freedom in the system scales as  $N \sim N_p N_\Delta$ . The  $O(N^2)$  scaling above assumes an iterative solution of the discretized system of equations, where the number of iterations is independent of  $N$ ; a direct solution will result in a scaling of  $O(N^3)$ , while a system size dependent number of iterations with an iterative solution results in a scaling higher than  $O(N^2)$ ; the worst case scaling being  $O(N^3)$ . The  $O(N^2)$  scaling is usually prohibitive, such that it precludes a numerical study of large system sizes. It is therefore not surprising that many of the past studies have been limited to an  $O(1)$  number of particles.

To overcome these limitations, there have been several efforts to develop *accelerated* techniques, where an accelerated technique is assumed to give a scaling closer to the ideal  $O(N)$ , while being sufficiently accurate at the same time. These accelerated techniques employ either some variant of the particle-particle-particle-mesh (P<sup>3</sup>M) method [9], or the Fast Multipole Method (FMM) [20]. One of the earliest Stokes flow boundary integral implementation with acceleration was perhaps presented by Greengard et al. [18], who employed the FMM for acceleration in complex domains. Using the particle-mesh-Ewald (PME) method, Metsi [46] developed an accelerated implementation of the Stokes flow boundary integral method for her studies on two dimensional periodic suspensions of emulsions and foams. Zinchenko and Davis [64, 65] employed multipole expansion accelerated boundary integral method to study large number of drops in a periodic geometry under shear. Freund [16] used the smooth particle-mesh-Ewald method to study the motion of periodic suspensions of RBCs and leukocytes in two dimensions; this was later extended to three dimensions by Zhao

et al. [63]. In the latter study [63], the effect of confinement was incorporated by explicitly discretizing the walls, which generally has unknown tractions and known no-slip velocity conditions. This explicit discretization is necessary because the periodic Green's function does not inherently satisfy the no-slip condition on the walls. Additionally, the previous authors employed a staggered time integrator, such that the wall tractions and the particle surface velocities were not determined simultaneously; this is due to the large cost associated with their simultaneous solution. Another potential drawback with the periodic Green's function is that it has a zero mean flow and a non-zero mean pressure gradient associated with it [22]. As a consequence, the pressure drop in the system is not directly a specified quantity, and must be solved for by varying the mean flow, which is a specified quantity [16, 63]. Note that many experiments on pressure driven flow have a specified pressure drop, and it is therefore desired to specify the pressure drop directly in numerical simulations without incurring additional computational costs. We also remark that the specified mean flow includes the flow outside the walls, as that is a part of the simulation box [63]; consequently, in such a method, neither the mean flow between the walls nor the pressure drop is a directly controlled quantity. Other recent work of possible interest is Rahimian et al. [52], where a FMM accelerated boundary integral method is presented. While this implementation was developed for an arbitrary domain, its applicability is restricted to two dimensional systems. In a subsequent article [62], the previous authors generalized their implementation to three dimensions, though only an unbounded domain was considered. At this point, it must be emphasized that all the prior accelerated implementations of the boundary integral method are based on either the free space Green's function or the periodic Green's function; in such a case, the boundaries of the confined domain are required to be explicitly discretized.

We next discuss previous boundary integral implementations employing the Green's function for the geometry of interest. Such a Green's function satisfies the appropriate boundary conditions at the domain boundaries; consequently, the unknowns at the domain boundaries, e.g. hydrodynamic tractions, do not enter the boundary integral equation. A popular geometry for which several boundary integral implementations have been developed is a slit – the region between two parallel walls. The Green's function for this geometry has been provided by Liron and Mochon [42]. A boundary integral implementation based on this Green's function was developed by Staben et al. [58] for rigid particles. This was later extended by Griggs et al. [21] for studies on drops in the same geometry. In a related work, Janssen and Anderson [27] also implemented a boundary integral method for drops between two parallel walls, though that was restricted to matched continuous and dispersed phase viscosities. This was later extended by Janssen and Anderson [28] to include non-matched viscosity problems. It is important to emphasize that none of these implementations are accelerated and have a computational cost of at least  $O(N^2)$ . Consequently, it is not surprising that all of the studies described above were limited to a few particles and are thus not suitable for studying suspension dynamics.

We now briefly discuss examples of other numerical techniques employed in the literature for studies on

the flow behavior of particles under confinement. One such simulation technique is the immersed boundary method, which has been employed, e.g. by Doddi and Bagchi [11] and Pranay et al. [51], for studies on capsules in a slit. Another popular technique is the lattice-Boltzmann method. As an example, MacMeccan et al. [44] developed a coupled lattice-Boltzmann and finite element method to study deformable particles, which included studies under confinement. A somewhat related algorithm is the multiparticle collision dynamics, which has been used by, e.g., Noguchi and Gompper [48] to study RBCs and vesicles in capillaries. The ideal computational cost of all the above numerical techniques is  $O(N)$ . Finally, Swan and Brady [60] have developed an accelerated Stokesian dynamics method for rigid spherical particles in a slit that uses ideas related to those presented here and scales as  $O(N \log N)$ .

In the present study, we develop an accelerated boundary integral method for multiphase flow in an arbitrary geometry and implement it for a slit geometry as shown in Fig. 1. The computational complexity of this algorithm scales as  $O(N)$  or  $O(N \log N)$  depending on the specific numerical scheme employed. The latter scaling of  $O(N \log N)$  is associated with the use of fast Fourier transforms (FFTs) if one or more directions have periodic boundary conditions, though that is not a requirement of our method. In the present effort, we provide a detailed description using the example of the slit geometry; its extension to other geometries is straightforward. The acceleration in our method is provided by the use of General Geometry Ewald-Like Method (GGEM) [24]. The choice of GGEM as the acceleration technique necessitates the use of an alternative boundary integral formulation in which the velocity field is expressed solely in terms of a single layer integral [50]; its unknown density is obtained from a second kind integral equation involving the double layer integral. The resulting single and double layer integrals are computed efficiently employing the GGEM methodology, which results in the aforementioned favorable scaling of  $O(N)$  or  $O(N \log N)$ .

The organization of this article is as follows. In Sec. (2), we provide a brief overview of the GGEM accelerated boundary integral method and also discuss some of the limitations of the current implementation. Following this, in Sec. (3), we present the boundary integral formulation and discuss its numerical implementation using GGEM. In Sec. (4), we present the procedure to compute the hydrodynamic traction jump at a particle surface using the example of a capsule with a neo-Hookean membrane. The solution procedure for the discretized boundary integral equation is presented next in Sec. (5). An extensive validation of our method is presented in Sec. (6). Lastly, in Sec. (7), we present results from several large scale multiparticle simulations and verify the computational complexity of our algorithm.

## 2. Overview of the current work

We summarize here some of the key aspects of the present work. Each of these points are discussed further later in the article.

- The general geometry Ewald like method (GGEM) employed in the current work for acceleration

essentially yields the *geometry-dependent* Green’s function and other associated quantities. This work is a first instance of an accelerated boundary integral method based on the geometry-dependent Green’s function. Prior implementations have employed either the free-space Green’s function (in case of FMM accelerated methods) or the periodic Green’s function (in case of PME accelerated methods).

- The GGEM methodology decomposes the overall problem into a *local* problem and a *global* problem, essentially by splitting the Green’s function into local (singular but exponentially-decaying) and global (smooth but long-ranged) parts. The implementation of the local problem is similar to that of the traditional boundary integral method. However, since the local Green’s function decays exponentially with distance from the source of the singularity, distant elements are not coupled and the local solution can be obtained in  $O(N)$  operations.
- The global problem involves solving a *single* phase Stokes equation in the domain of interest with known boundary conditions and with a known smooth distribution of force densities. It is in this problem that the coupling between distant elements appears. In solving the global problem, one is not concerned with the particle interfaces, or the different viscosity fluids present inside and outside the particle (if that is the case in the original problem). This major simplification allows the use of a wide variety of fast and accurate numerical techniques present in the literature for the solution of Navier-Stokes equation in an arbitrary domain. All these methods, including those based on finite difference, finite volume, finite element, and spectral methods are suitable here [6, 7, 12, 14]. In addition, various fast and efficient implementations of Navier-Stokes solvers on GPUs and distributed memory systems are readily available [23, 61].
- We present a spectral  $O(N \log N)$  Stokes flow solver for the global problem in a slit geometry, which, as indicated in the introduction, is one of the most widely-studied confined geometries studied in the literature. This solver employs a Fourier-Chebyshev Galerkin method in conjunction with the influence matrix approach [7]. The unknown coefficients of the Fourier-Chebyshev series expansion are computed with a direct  $O(N)$  algorithm – no iterations are necessary here, as would be the case with FMM or PME accelerated methods in a slit.

The implementation of the methodology presented in this paper also has some limitations. An important limitation of the current implementation concerns the evaluation of the near singular integrals – these integrals arise when the gaps between the particles become very small, and, if not treated appropriately, may cause the simulations to diverge. In the present work this is alleviated by requiring that the minimum interparticle gap in the system be always maintained above a specified value; this is achieved by the use of an overlap correction procedure in an auxiliary step. There are several other minor limitations of the current implementation. For example, we currently use linear elements to discretize the particle surface. It may be

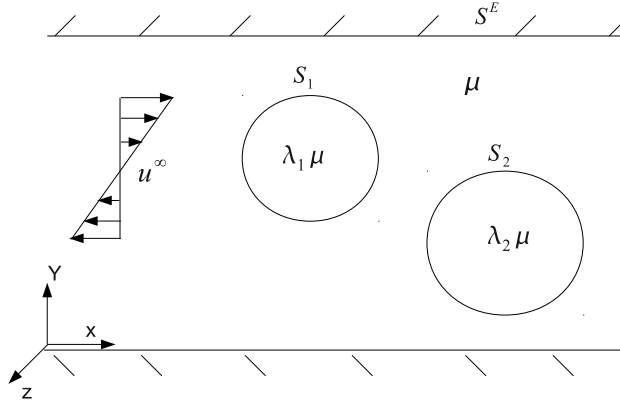


Figure 1: Schematic of the problems considered here: a dispersed phase with viscosity  $\mu$  inside the domain boundaries denoted by  $S^E$ , containing (for example) two particles with internal viscosities  $\lambda_1\mu$  and  $\lambda_2\mu$  respectively; their surfaces are denoted by  $S_1$  and  $S_2$ . The undisturbed flow is denoted by  $\mathbf{u}^\infty$ .

beneficial to employ higher order discretizations, like a spectral discretization, which could be particularly helpful for the accurate evaluation of the near singular integrals. In this paper results are reported only for a slit geometry. It will be appropriate to develop efficient implementations of our methodology for other geometries like a cylinder. It must be emphasized that none of the above limitations are inherent to our methodology and we hope to address these in future efforts.

### 3. Problem Formulation and Implementation

#### 3.1. Boundary integral equation for fluid motion

We consider a three-dimensional suspension of deformable particles (e.g. fluid-filled capsules) as shown in Fig. (1), where both the suspending fluid and the fluid enclosed by the particles are assumed to be Newtonian and incompressible. The viscosity of the suspending fluid is taken to be  $\mu$ , while the viscosity of fluid enclosed by capsule  $m$  is taken to be  $\lambda_m\mu$ , such that  $\lambda_m$  is the viscosity ratio of the interior and the exterior fluid for this particular capsule. The Reynolds number for the problem is assumed to be sufficiently small that the fluid motion is governed by the Stokes equation. Under these assumptions, one may write the velocity at any point in the domain with an integral expression involving only the boundary of the particles [50]. We first introduce the formulation that is most commonly used,

$$\begin{aligned}
 u_j(\mathbf{x}_0) = & \frac{2}{1 + \lambda_m} u_j^\infty(\mathbf{x}_0) - \frac{1}{4\pi\mu(1 + \lambda_m)} \sum_{n=1}^{N_p} \int_{S^n} \Delta f_i(\mathbf{x}) G_{ji}(\mathbf{x}_0, \mathbf{x}) dS(\mathbf{x}) \\
 & + \frac{1}{4\pi(1 + \lambda_m)} \sum_{n=1}^{N_p} (1 - \lambda_n) \int_{S^n} u_i(\mathbf{x}) T_{ijk}(\mathbf{x}, \mathbf{x}_0) n_k(\mathbf{x}) dS(\mathbf{x}),
 \end{aligned} \tag{1}$$

where  $\mathbf{u}(\mathbf{x}_0)$  is the fluid velocity at a point  $\mathbf{x}_0$  lying on the boundary of particle  $m$  (i.e.  $\mathbf{x}_0 \in S^m$ ,  $S^m$  denotes the surface of particle  $m$ ),  $\mathbf{u}^\infty(\mathbf{x}_0)$  is the undisturbed fluid velocity at the point  $\mathbf{x}_0$ ,  $\Delta \mathbf{f}(\mathbf{x})$  is the

hydrodynamic traction jump across the interface [50], and the sums are over all the  $N_p$  particles in the system. The Green's function and its associated stress tensor are denoted by  $\mathbf{G}$  and  $\mathbf{T}$  respectively in the above equation, and integrals involving them as the kernel are typically referred to as the single layer integral and the double layer integral respectively [30, 50]. From here onwards, a principal value of the double layer integral over a part of the boundary is assumed whenever the target point  $\mathbf{x}_0$  lies on that boundary. For example, in the above equation, the double layer integral over  $S^n$  is assumed to denote the principal value when  $n = m$ . A crucial aspect of the above formulation is that the Green's function  $\mathbf{G}$  and associated stress tensor  $\mathbf{T}$  are taken to satisfy the boundary conditions imposed at the system boundaries, so the integrals above only involve the internal (interfacial) boundaries; if the Green's function for any other geometry is employed (e.g. periodic), additional integrals over the domain boundaries arise in Eq. (1).

The above form of the boundary integral equation (1), using the free space Green's function (the Oseen-Burgers tensor) or the Green's function for a triply periodic domain given by Hasimoto [22] is widely used in the literature and is the basis for numerous numerical implementations, including the references cited in the introduction. However, for reasons that will be discussed shortly, this form is not amenable to numerical solution by an accelerated method in an arbitrary domain when using the Green's function for that domain. In the present effort, therefore, we employ an alternative formulation in which the fluid velocity is expressed solely in terms of the single layer integral with density  $\mathbf{q}(\mathbf{x})$  as follows:

$$u_j(\mathbf{x}_0) = u_j^\infty(\mathbf{x}_0) + \sum_{n=1}^{N_p} \int_{S^n} q_i(\mathbf{x}) G_{ji}(\mathbf{x}_0, \mathbf{x}) dS(\mathbf{x}). \quad (2)$$

The single layer density  $\mathbf{q}(\mathbf{x}_0)$  satisfies (for  $\mathbf{x}_0 \in S^m$ )

$$q_j(\mathbf{x}_0) + \frac{\kappa_m}{4\pi} n_k(\mathbf{x}_0) \sum_{n=1}^{N_p} \int_{S^n} q_i(\mathbf{x}) T_{jik}(\mathbf{x}_0, \mathbf{x}) dS(\mathbf{x}) = -\frac{1}{4\pi\mu} \left( \frac{\Delta f_j(\mathbf{x}_0)}{\lambda_m + 1} + \kappa_m f_j^\infty(\mathbf{x}_0) \right), \quad (3)$$

where  $\kappa_m$  is defined as

$$\kappa_m = \frac{\lambda_m - 1}{\lambda_m + 1}, \quad (4)$$

while  $\mathbf{f}^\infty$  is the traction at a given point (computed with the suspending fluid viscosity  $\mu$ ) due to the stress generated in the fluid corresponding to the undisturbed flow  $\mathbf{u}^\infty$  (see Appendix B for examples). In Appendix A, this formulation is derived from the Lorentz reciprocal theorem for the case of a single particle. This derivation follows closely the approach outlined in Chap. (5) of Pozrikidis [50] and is provided here for completeness.

We now clarify the motivation for employing Eqs. (2) and (3) rather than the more commonly employed formulation in Eq. (1). We begin by noting that the first argument  $\mathbf{x}_1$  of  $\mathbf{G}(\mathbf{x}_1, \mathbf{x}_2)$  and  $\mathbf{T}(\mathbf{x}_1, \mathbf{x}_2)$  denotes the field (target) point of the functions, while the second argument  $\mathbf{x}_2$  denotes the location of the pole (source) of the singularity that drives the flow. A close look at Eq. (1) reveals that the operand of  $\mathbf{G}(\mathbf{x}_0, \mathbf{x})$ ,

$\Delta f_i(\mathbf{x})$ , is a function of the position of the pole of the singularity ( $\mathbf{x}$ ) and that the field point of the  $\mathbf{G}$  tensor is same as the target point of the overall boundary integral equation ( $\mathbf{x}_0$ ). In other words, the operand of  $\mathbf{G}$  is independent of its target point, and consequently the same collection of point forces can be used to compute the velocity at any target point. This requirement is essential to any accelerated method, as in such methods a part of the calculation gives the velocity (or other relevant quantities) simultaneously at *all* target points (e.g., boundary element nodes) due to *all* the singularities present in the system. This is possible only if the operands of the singularities are independent of the target points of the singularities, and instead are functions of the location of the pole of the respective singularities.

With this aspect clarified, it is seen that this important condition is not satisfied for the double layer kernel  $\mathbf{T}(\mathbf{x}, \mathbf{x}_0)$  in Eq. (1) as its multiplicands  $\mathbf{u}(\mathbf{x})$  and  $\mathbf{n}(\mathbf{x})$  are functions of its target point  $\mathbf{x}$ . Also note that no general relationship exists that would allow one to switch the location of the pole and the field points in  $\mathbf{T}$ . (This is possible for  $\mathbf{G}$ , since, by self-adjointness,  $G_{ij}(\mathbf{x}, \mathbf{x}_0) = G_{ji}(\mathbf{x}_0, \mathbf{x})$  [50]). Hence the above formulation (1) is not suitable for our purposes here, though it can still be used for problems in which the viscosity ratio is unity, as the double layer integral vanishes in such a case [51]. In contrast, in the formulation employed in this work (Eqs. 2 and 3), the multiplicand  $\mathbf{q}(\mathbf{x})$  of both  $\mathbf{G}(\mathbf{x}_0, \mathbf{x})$  and  $\mathbf{T}(\mathbf{x}_0, \mathbf{x})$  is a function of the location of the source point  $\mathbf{x}$ . Hence, it is amenable to numerical solution by an accelerated method.

We now describe the fast computation of the velocity and pressure fields due to a collection of known point forces, which is closely related to the problem of computing the Green's function and its associated stress tensor in the geometry of interest. Later in Secs. (3.4) and (3.5), we employ this technique to compute the single layer and double layer integrals.

### 3.2. GGEM Stokes flow solver for a collection of point forces

Consider the velocity field  $\mathbf{u}(\mathbf{x})$  and the pressure field  $p(\mathbf{x})$  due to a collection of  $N_s$  point forces, such that the strength and location of the  $\nu^{th}$  point force are given by  $\mathbf{g}^\nu$  and  $\mathbf{x}^\nu$  respectively. The velocity and pressure fields above are obtained from the solution of the Stokes and the continuity equation as shown below:

$$-\nabla p(\mathbf{x}) + \mu \nabla^2 \mathbf{u}(\mathbf{x}) + \sum_{\nu=1}^{N_s} \mathbf{g}^\nu \delta(\mathbf{x} - \mathbf{x}^\nu) = 0, \quad (5a)$$

$$\nabla \cdot \mathbf{u}(\mathbf{x}) = 0, \quad (5b)$$

and subject to given boundary conditions on the system boundary  $S^E$ . By definition, the above velocity and pressure fields along with the associated stress tensor  $\boldsymbol{\sigma}$  can be written in terms of a Green's function

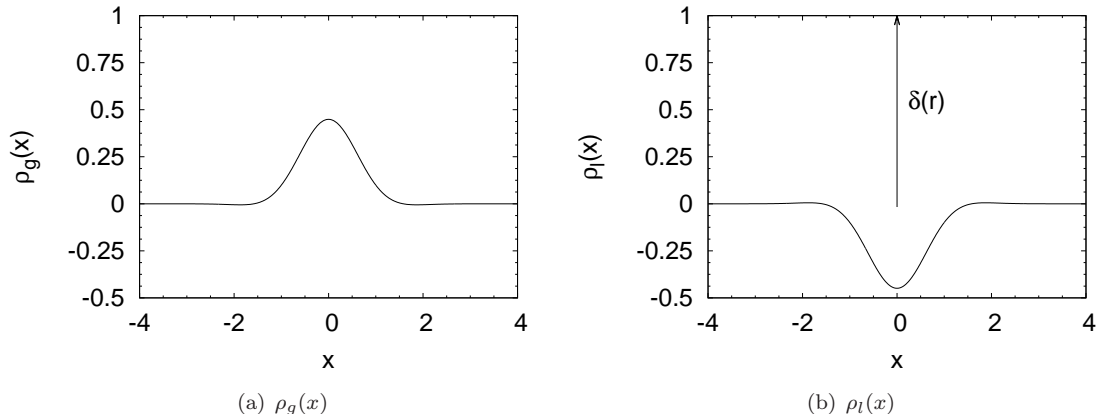


Figure 2: Variation of the global  $\rho_g(x)$  and the local  $\rho_l(x)$  force density along the  $x$ -axis, given the center of the force density is at the origin. Note that both of these densities are functions only of the distance  $r$  from the origin (see Eq. 8). Also note that  $\rho_g(\mathbf{r}) + \rho_l(\mathbf{r}) = \delta(\mathbf{r})$ . In numerical calculations, we set  $\rho_g(\mathbf{r}) = 0$  for  $r > 4/\alpha$ . For plotting  $\rho_g(x)$  and  $\rho_l(x)$  here, we set  $\alpha = 1$ .

$\mathbf{G}$ , its pressure vector  $\mathbf{P}$  and stress tensor  $\mathbf{T}$  as

$$u_i(\mathbf{x}) = \frac{1}{8\pi\mu} \sum_{\nu=1}^{N_s} G_{ij}(\mathbf{x}, \mathbf{x}^\nu) g_j^\nu, \quad (6a)$$

$$p(\mathbf{x}) = \frac{1}{8\pi} \sum_{\nu=1}^{N_s} P_j(\mathbf{x}, \mathbf{x}^\nu) g_j^\nu, \quad (6b)$$

$$\sigma_{ik}(\mathbf{x}) = \frac{1}{8\pi} \sum_{\nu=1}^{N_s} T_{ijk}(\mathbf{x}, \mathbf{x}^\nu) g_j^\nu. \quad (6c)$$

The stress tensor  $T_{ijk}$  in the above equation is obtained from  $G_{ij}$  and  $P_j$  from the Newtonian constitutive equation

$$T_{ijk}(\mathbf{x}, \mathbf{x}^\nu) = -P_j(\mathbf{x}, \mathbf{x}^\nu) \delta_{ik} + \mu \left( \frac{\partial G_{ij}(\mathbf{x}, \mathbf{x}^\nu)}{\partial x_k} + \frac{\partial G_{kj}(\mathbf{x}, \mathbf{x}^\nu)}{\partial x_i} \right). \quad (7)$$

A close look at the boundary integral equations (2) and (3) shows that to evaluate the integrals we do not explicitly need the Green's function  $\mathbf{G}$  and its stress tensor  $\mathbf{T}$  but only their products with the density  $\mathbf{q}$ . Put simply, our end goal is to quickly find in time  $O(N_s)$  or  $O(N_s \log N_s)$  the velocity  $\mathbf{u}$  and the stress tensor  $\boldsymbol{\sigma}$  due to a given set of point forces – explicit construction of  $\mathbf{G}$  and  $\mathbf{T}$  are not necessary.

One of the attractive features of the method presented here lies in the fact that it is applicable to an *arbitrary* geometry. For simplicity and considering the interest of the present work, we provide a detailed discussion only for a slit geometry (see Fig. 6); generalization of the formalism for an arbitrary geometry is straightforward [25]. For the present slit domain, there is a no slip boundary condition at the two rigid walls at  $y = 0$  and  $y = H$ , while periodic boundary conditions are assumed in the other two directions  $x$  and  $z$ , with spatial periods  $L_x$  and  $L_z$ , respectively.

To achieve the computational complexity of  $O(N_s \log N_s)$  alluded to above, we employ the general geom-

etry Ewald like method (GGEM) [24] for computing the velocity and stress fields due to a given collection of point forces. We briefly describe GGEM next. In the GGEM methodology, the Dirac-delta density in Eq. (5) is expressed as the sum of a smoothly varying quasi-Gaussian *global* density  $\rho_g(\hat{\mathbf{r}})$  characterized by a “splitting parameter”  $\alpha$  and a second *local* density  $\rho_l(\hat{\mathbf{r}})$  (see Fig. 2). Here  $\hat{\mathbf{r}}$  is a position vector relative to the pole of the singularity,  $\hat{\mathbf{r}} = \mathbf{x} - \mathbf{x}^\nu$ . The above global and local densities are respectively given by the following expressions:

$$\rho_g(\hat{\mathbf{r}}) = \frac{\alpha^3}{\pi^{3/2}} e^{-\alpha^2 \hat{r}^2} \left( \frac{5}{2} - \alpha^2 \hat{r}^2 \right), \quad (8a)$$

$$\rho_l(\hat{\mathbf{r}}) = \delta(\hat{\mathbf{r}}) - \rho_g(\hat{\mathbf{r}}), \quad (8b)$$

where  $\alpha^{-1}$  represents a length scale over which the delta-function density has been smeared using the quasi-Gaussian form above, and consequently it also represents the length scale beyond which both the global and the local densities are effectively zero. It is important to emphasize that the total density remains a  $\delta$ -function, i.e.  $\rho_g(\hat{\mathbf{r}}) + \rho_l(\hat{\mathbf{r}}) = \delta(\hat{\mathbf{r}})$ . The motivation for this particular splitting of the  $\delta$ -function density into  $\rho_g(\hat{\mathbf{r}})$  and  $\rho_l(\hat{\mathbf{r}})$  will be obvious below.

We next consider the solution of the Stokes and continuity equation with the above two force densities as forcing functions. The solution driven by the local density,  $\mathbf{u}^l(\mathbf{x})$ ,  $p^l(\mathbf{x})$ , and  $\boldsymbol{\sigma}^l(\mathbf{x})$  (velocity, pressure, and stress respectively) will be referred to as the local solution, and satisfies the local problem

$$-\nabla p^l(\mathbf{x}) + \mu \nabla^2 \mathbf{u}^l(\mathbf{x}) + \sum_{\nu=1}^{N_s} \mathbf{g}^\nu \rho_l(\mathbf{x} - \mathbf{x}^\nu) = 0, \quad (9a)$$

$$\nabla \cdot \mathbf{u}^l(\mathbf{x}) = 0. \quad (9b)$$

This equation will be solved in an unbounded domain, i.e. the solution decays to zero at infinity. The solution  $\mathbf{u}^g(\mathbf{x})$ ,  $p^g(\mathbf{x})$ , and  $\boldsymbol{\sigma}^g(\mathbf{x})$  driven by the global density will be referred to as the global solution, and satisfies the global problem

$$-\nabla p^g(\mathbf{x}) + \mu \nabla^2 \mathbf{u}^g(\mathbf{x}) + \sum_{\nu=1}^{N_s} \mathbf{g}^\nu \rho_g(\mathbf{x} - \mathbf{x}^\nu) = 0, \quad (10a)$$

$$\nabla \cdot \mathbf{u}^g(\mathbf{x}) = 0. \quad (10b)$$

The boundary conditions for the global problem are set so that the total velocity field  $\mathbf{u}(\mathbf{x}) = \mathbf{u}^l(\mathbf{x}) + \mathbf{u}^g(\mathbf{x})$  satisfies the specified boundary conditions for the overall problem. Once the local and the global solutions are known, the solution to the overall problem is obtained as

$$\mathbf{u}(\mathbf{x}) = \mathbf{u}^l(\mathbf{x}) + \mathbf{u}^g(\mathbf{x}), \quad (11a)$$

$$p(\mathbf{x}) = p^l(\mathbf{x}) + p^g(\mathbf{x}), \quad (11b)$$

$$\boldsymbol{\sigma}(\mathbf{x}) = \boldsymbol{\sigma}^l(\mathbf{x}) + \boldsymbol{\sigma}^g(\mathbf{x}). \quad (11c)$$

We next discuss the solution procedures for the local and the global problems.

### 3.2.1. Local solution

Consider first the local problem. The solution to this problem,  $\mathbf{u}^l(\mathbf{x})$ ,  $p^l(\mathbf{x})$ , and  $\boldsymbol{\sigma}^l(\mathbf{x})$  is expressed by a set of equations similar to that in Eqs (6), which, for the simplicity of nomenclature, is called the local Green's function  $\mathbf{G}^l$  and its associated quantities. In short, we append the superscript  $l$  to the previously defined quantities to denote the solution associated with the local density as the forcing function, and these are given by the following:

$$G_{ij}^l(\mathbf{x}, \mathbf{x}^\nu) = \left( \frac{\delta_{ij}}{\hat{r}} + \frac{\hat{x}_i \hat{x}_j}{\hat{r}^3} \right) \text{erfc}(\alpha \hat{r}) - \frac{2\alpha}{\sqrt{\pi}} \left( \delta_{ij} - \frac{\hat{x}_i \hat{x}_j}{\hat{r}^2} \right) e^{-\alpha^2 \hat{r}^2}, \quad (12a)$$

$$P_j^l(\mathbf{x}, \mathbf{x}^\nu) = \frac{2\hat{x}_j}{\hat{r}^3} \text{erfc}(\alpha \hat{r}) + \frac{4\alpha \hat{x}_j}{\sqrt{\pi}} \left( \frac{1}{\hat{r}^2} - \alpha^2 \right) e^{-\alpha^2 \hat{r}^2}, \quad (12b)$$

$$T_{ijk}^l(\mathbf{x}, \mathbf{x}^\nu) = -\frac{6\hat{x}_i \hat{x}_j \hat{x}_k}{\hat{r}^5} \text{erfc}(\alpha \hat{r}) - \frac{12\alpha}{\sqrt{\pi}} \frac{\hat{x}_i \hat{x}_j \hat{x}_k}{\hat{r}^4} e^{-\alpha^2 \hat{r}^2} \\ + \frac{4\alpha^3}{\sqrt{\pi}} \left( \delta_{jk} \hat{x}_i + \delta_{ik} \hat{x}_j + \delta_{ij} \hat{x}_k - \frac{2\hat{x}_i \hat{x}_j \hat{x}_k}{\hat{r}^2} \right) e^{-\alpha^2 \hat{r}^2}, \quad (12c)$$

where  $\hat{\mathbf{x}} = \mathbf{x} - \mathbf{x}^\nu$ , while  $\hat{r} = |\hat{\mathbf{x}}|$ . The velocity and stress fields are then obtained as:

$$u_i^l(\mathbf{x}) = \frac{1}{8\pi\mu} \sum_{\nu=1}^{N_s} G_{ij}^l(\mathbf{x}, \mathbf{x}^\nu) g_j^\nu, \quad (13a)$$

$$\sigma_{ik}^l(\mathbf{x}) = \frac{1}{8\pi} \sum_{\nu=1}^{N_s} T_{ijk}^l(\mathbf{x}, \mathbf{x}^\nu) g_j^\nu. \quad (13b)$$

The solution in Eq. (12) has been obtained with *free-space* boundary conditions, i.e. all of them decay to zero at infinity. In other words, the local solution is independent of the geometry of interest. The violation of the boundary condition requirements of the domain by employing free space boundary conditions above will be corrected by appropriately choosing the boundary conditions for the flow problem associated with the global force densities as the forcing function.

An important observation at this point is that the local solutions in (12) are short ranged, decaying approximately as  $e^{-\alpha^2 \hat{r}^2}$ . Consequently, the contribution from the local solution can be neglected beyond a length scale  $\sim \alpha^{-1}$  from the origin of the corresponding local density. In this work, this cutoff length was taken as  $r_{cut} = 4/\alpha$  throughout. The near neighbor list required for the efficient computation of the local solution is generated by the  $O(N_s)$  cell-linked list algorithm [1].

It is important to point out that the  $\mathbf{G}^l$  in Eq. (12a) has the same functional form as the real space term in the periodic Stokeslet (Green's function) provided by Hasimoto [22]. In other words, Hasimoto's solution for the periodic Stokeslet can also be obtained by first splitting the  $\delta$ -function density into the local

and global densities as in Eq. (8); the local problem is then solved as described above, while the global problem is solved with a Fourier Galerkin method with the appropriate assumptions described in Hasimoto [22]. Since PME accelerated methods (e.g. [34]) for Stokes flow employ the periodic Stokeslet given by Hasimoto [63], this observation illustrates a connection between PME like methods and GGEM. A very important distinction, though, is that the performance of PME like methods is tied to the use of discrete Fourier transforms and thus periodic domains, which is not the case with GGEM (discussed below) and hence the latter’s much broader applicability.

### 3.2.2. Global solution

We now describe the solution to the global problem, i.e. the flow problem associated with the collection of global force densities. We first discuss the boundary conditions for the global problem. As was mentioned earlier, the overall solution for a given collection of point forces is the sum of the corresponding quantities from the local and the global solutions, see Eq. (11). It is obvious that the same should be true for boundary conditions. Consequently, to satisfy any type of boundary condition (e.g. Dirichlet) at an arbitrary location, we set the boundary condition for the global part so that its sum with the known contribution from the local part (above) adds up to the required value. Again, we employ the example of the slit geometry, noting that this scheme is equally applicable to other geometries. To satisfy the no-slip condition at the two rigid walls of the slit, we require the following at  $y = 0$  and  $y = H$ :

$$\mathbf{u}^g = -\mathbf{u}^l. \quad (14)$$

Note that in the present formulation the *static* no-slip condition is always imposed at the rigid walls for computing the velocity field due to the Green’s function (or point forces). This is true even in problems where the walls may not be at rest, a common example being simple shear flow. The effect of the undisturbed flow enters the boundary integral equation via  $\mathbf{u}^\infty$  and  $\mathbf{f}^\infty$  in Eqs. (2) and (3). To satisfy the periodic boundary conditions in  $x$  and  $z$  directions, we impose equivalent periodic boundary conditions in the global calculation. As far as the local solution is concerned, we require that it decays to a negligible value over a length scale equal to half of the spatial period in  $x$  and  $z$  directions or smaller: i.e.  $r_{cut} < L_x/2$  and  $r_{cut} < L_z/2$ . Given the above choice  $r_{cut} = 4/\alpha$ , we require that  $\alpha L_x > 8, \alpha L_z > 8$ . This fact, coupled with the minimum image convention [9] employed in the computation of the local solution ensures its periodicity.

Before proceeding further, we note that, in general, two subtleties arise in considering the behavior of the global solution near boundaries. The first is the issue of boundary shape. In the present work we take the boundary to be smooth on the scale of the suspended particle size. If that is not the case, it will be necessary to resolve the length scales of the boundary roughness. For such a boundary it might be convenient to revert to a conventional accelerated method and explicitly discretize the boundary. Alternately, in the present context, the global solution could be obtained using a locally-refined mesh near the domain boundary

to capture its features (see, e.g. Fard et al. [13]), without destroying the scaling of the method with the number of suspended particles.

Another issue arises in principle if a particle very closely approaches a (smooth) boundary. This does not arise in the context of the present application as deformable particles migrate away from solid surfaces in shear flow due to the hydrodynamic dipole interaction between the particle and the wall [57]. Nevertheless, it can happen in principle and leads to the situation where the boundary condition for the global problem that must be satisfied becomes nearly singular. This is because, at a no-slip boundary, we require  $\mathbf{u}^g = -\mathbf{u}^l$  and a point force a distance  $\epsilon$  away from the boundary leads to a local velocity  $\mathbf{u}^l$  of  $O(1/\epsilon)$  on the boundary. This situation can be addressed by adding the image system for a plane wall [5] (and splitting it into local and global parts), in which case the effects of the singularities cancel on the wall. See Swan and Brady [60] for a related discussion in the Stokesian dynamics context.

Having discussed the boundary conditions for the global problem, we turn to the solution procedure of the Stokes and the continuity equation with the given collection of global force densities as the forcing function; see Eq. (10). For an arbitrary geometry one may employ any desired discretization scheme for the solution of the global problem. If a finite difference or a finite element scheme is used, then the solution can be obtained at a cost of  $O(N)$  when the resulting sparse matrix equations are solved iteratively with proper preconditioners; the multigrid preconditioner for Stokes flow is an attractive choice [12, 56]. Section 7.2 contains further discussion of the scaling of computation time with problem size. For the slit problem of interest here, past work [25, 51] employed discrete Fourier series approximation in the periodic  $x$  and  $z$  directions, while a second order finite difference discretization was employed in the wall normal  $y$  direction. In the present work, we develop a fully spectral solution procedure by employing the discrete Chebyshev polynomial approximation [6] in the wall normal direction, while the discrete Fourier series approximation is used in the periodic  $x$  and  $z$  directions. For example, the  $x$ -component  $u^g$  of the global velocity  $\mathbf{u}^g = (u^g, v^g, w^g)$  in Eq. (10) is expressed as

$$u^g(\mathbf{x}) = \sum_{l=-N_x/2}^{N_x/2-1} \sum_{m=-N_z/2}^{N_z/2-1} \sum_{n=0}^{N_y-1} \hat{u}_{lmn}^g T_n(\bar{y}) e^{i2\pi lx/L_x} e^{i2\pi mz/L_z}, \quad (15)$$

where  $T_n(\bar{y}) = \cos(n \cos^{-1} \bar{y})$  is the Chebyshev polynomial of the  $n^{\text{th}}$  degree [6],  $\bar{y}$  represents the mapping from  $[0, H]$  to  $[-1, 1]$ :  $\bar{y} = 2y/H - 1$ , while  $N_x$ ,  $N_y$ , and  $N_z$  respectively denote the number of terms (modes) in the corresponding series approximation. Similar expressions are written for other components of the velocity and the pressure. An important implication of this representation, particularly with regard to the pressure, is that the pressure drop associated with this point force solution is always zero over the spatial period of the domain, while the mean flow is (in general) non-zero. This ensures that the pressure drop obtained from the boundary integral method always equals the pressure drop specified in the imposed bulk flow (i.e. in the absence of the particles). Returning to the expression in Eq. (15), we note that the use of

the Fourier series approximation in  $x$  and  $z$  directions ensures that the periodic boundary conditions in these directions are inherently satisfied. The Chebyshev polynomials, on the other hand, do not automatically satisfy the boundary conditions in the wall normal direction; the satisfaction of these boundary conditions was accomplished by employing the tau method [6, 49]. In the tau method, the equations for the highest two modes in the series approximation are replaced by equations representing the two boundary conditions; see, e.g., Canuto et al. [6] or Peyret [49] for details. An attractive feature of the discrete Chebyshev polynomial approximation is that FFTs can be used for rapidly transferring information from the physical to spectral space and vice-versa [7]. A major drawback, though, with solving differential equations with Chebyshev polynomial approximation is that the differentiation matrix is full in both the spectral and the physical space [49] (in contrast, the Fourier differentiation matrix is diagonal in the spectral space). Due to the full nature of the Chebyshev differentiation matrix, a straightforward implementation for solving the Stokes flow problem will lead to an  $O(N_y^3)$  method. For the incompressible Stokes flow problem here, though, an alternate approach exists in which the solution to the Stokes equation is obtained from the solution of a series of Helmholtz equations [7]. In this case, with a little manipulation, a quasi-tridiagonal system of equations results, for which a direct  $O(N_y)$  algorithm exists [49]. This approach for solving the incompressible Stokes equation, or more generally the incompressible Navier-Stokes equations, is popularly known in the literature as the Kleiser-Schumann influence matrix method [7]. A detailed discussion of this approach including the equations being solved and their respective boundary conditions is presented in Appendix C. Here we only sketch out the main computational aspects of this approach. To begin, each of variables appearing in the Stokes and the continuity equation are expanded in a truncated Fourier series in  $x$  and  $z$  directions; see, e.g., Eq. (15). These expressions are then substituted in the Stokes and the continuity equations. Subsequently, by the application of the Galerkin method, a set of coupled ordinary differential equations (ODE) in  $y$  is obtained for each of the Fourier modes of all the unknown variables (velocity components and pressure). These coupled ODEs are solved with the Chebyshev-tau influence matrix method, which involve Chebyshev transformations, quasi-tridiagonal matrix equation solves, and inverse Chebyshev transformations in that order. The solution thus obtained yields the Fourier coefficients of the velocity components and the pressure. An inverse Fourier transform then leads to the solution for the velocity and the pressure in the physical space. The computation of the stress tensor  $\sigma^g$  requires the derivatives of the velocities; these differentiations are performed in the transform space [6, 49]. All of the above Fourier and the Chebyshev transforms along with their inverse transforms are performed using the FFT algorithm. Thus, the asymptotic computational cost of the solution procedure for the global problem scales as  $N \log N$ , where  $N = N_x N_y N_z$ . Assuming  $N \sim N_s$  (see Sec. 7.2), we obtain the asymptotic computational cost of the global solution as  $O(N_s \log N_s)$ . A further discussion on the computational complexity of the algorithm is provided in Sec. (7.2).

We next introduce some of the important parameters associated with this solution procedure. Associated with each of the  $N_x$  and  $N_z$  Fourier modes, there are  $N_x$  and  $N_z$  equispaced trapezoidal quadrature points;

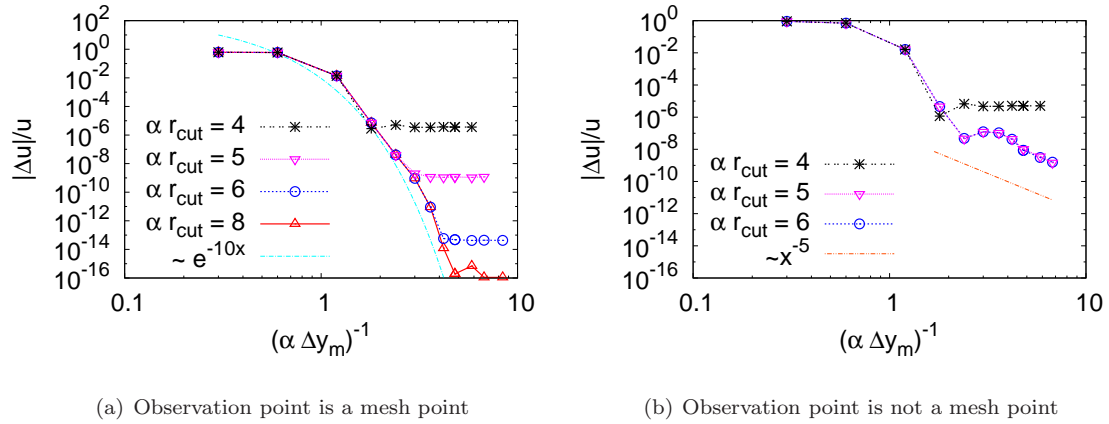


Figure 3: Relative error in the velocity ( $\Delta u/u$ ) due to a point force at a given observation point in a slit geometry with  $L_x = H = L_z = L$ . The abscissa in the plots is  $(\alpha \Delta y_m)^{-1}$ , while different curves are for different values of  $r_{cut}$  as labeled in the key. The strength of the point force is given by  $(F, F, F)$ , while its coordinates are  $(0.25L, 0.25L, 0.25L)$ . (a) The observation point is  $(0.5L, 0.5L, 0.5L)$ , which is always maintained on a mesh point, and (b) the observation point is  $(0.4312L, 0.3734L, 0.5234L)$  which is not a mesh point. In (a) we also plot the function  $y \sim e^{-10x}$  (chosen to closely match other curves on the plot) to demonstrate the exponential convergence of the solution, while in (b) we plot the function  $y \sim x^{-5}$  to demonstrate the algebraic convergence due to dominant interpolation errors at higher values of  $(\alpha \Delta y_m)^{-1}$ .

the corresponding spacings are denoted by  $\Delta x_m = L_x/N_x$  and  $\Delta z_m = L_z/N_z$ . Similarly, associated with the  $N_y$  Chebyshev polynomials, there are  $N_y$  Chebyshev Gauss-Lobatto quadrature points, the  $j^{th}$  of which is given by  $y_j = H/2(1 + \cos(\pi(j-1)/(N_y-1)))$ ; the mean mesh spacing in this case is denoted by  $\Delta y_m = H/(N_y-1)$ . Unless otherwise mentioned, the mean mesh spacings in all three directions are kept equal in simulations, i.e.  $\Delta x_m = \Delta y_m = \Delta z_m$ . For computing any of the above transforms, the value of the corresponding physical variable is required only at the corresponding quadrature points. Likewise, as is customary, the final solution for the velocity, pressure and stress are also computed only at these quadrature points. This last step is essential in maintaining the optimal computational complexity of  $O(N \log N)$  alluded to above. The velocity and stress at any point not on the mesh is obtained via interpolation; here we employ 4<sup>th</sup> order Lagrange interpolation for which the error decays as  $h^5$ , where  $h$  is the characteristic mesh spacing. The error, therefore, is expected to decay exponentially fast with the number of modes for any point on the mesh, while it is expected to decay as  $h^5$  for any point not on the mesh. It is appropriate to point out here that exponential convergence of the solution is possible even at a non-mesh point while maintaining the computational complexity of  $O(N \log N)$  – this can be achieved by employing the basic principles of non-uniform FFT calculations; see, e.g., [19, 40] for details.

### 3.2.3. Convergence of the GGEM solution

We demonstrate next the convergence behavior of the GGEM Stokes flow solution presented above. It will be helpful to begin this section with a discussion of various sources of error in the solution procedure. It should be obvious that the overall error in the solution results from errors in both the local and the global solution procedures. The error in the local solution arises due to its truncation beyond a distance

of  $r_{cut}$  from the source of the singularity – this error scales as  $e^{-\alpha^2 r_{cut}^2}$  (Sec. 3.2.1, [40]). Typically, we set  $r_{cut} = 4/\alpha$ , which is expected to result in an error of  $O(10^{-7})$ . Smaller error in the local solution can be obtained by increasing the value of  $r_{cut}$ . The error in the global solution has three different sources. The first source of error is the truncation of the Fourier-Chebyshev series expansion at some finite number of modes; see Eq. (15). The error due to this truncation is expected to decay exponentially fast on the mesh points with the parameter  $(\alpha\Delta y_m)^{-1}$  – this convergence rate results due to the spectral nature of the global solution procedure employed here. For other solution procedures, such as a finite difference scheme [25, 51], an algebraic convergence with the parameter  $(\alpha\Delta y_m)^{-1}$  will be obtained. Next, for any point not on the mesh, the global solution has to be obtained by interpolation from nearby mesh points, which introduces an additional error scaling as  $(\alpha\Delta y_m)^5$  in the current work. Lastly, there is also an error associated with the assignment of the global force density on the mesh points – this is required for computing its Fourier and Chebyshev transforms. The global density decays approximately as  $e^{-(\alpha r)^2}$  with distance  $r$  from the origin of the density (Eq. 8a). Therefore, just like the local solution, we truncate the global density beyond a distance of  $r_{cut} = 4/\alpha$  from the origin of the singularity. It is expected that the error due to this truncation will scale as  $e^{-(\alpha r_{cut})^2}$ . Again, a smaller truncation error can be obtained by setting a larger value of  $r_{cut}$  – in such cases the cost associated with the global force density assignment on the mesh points can be large and the fast Gaussian gridding algorithm [19, 40, 41] is recommended.

Having discussed the various sources of errors in the solution procedure, we turn to verifying the expected convergence behavior with a test problem. In this test problem, we compute the velocity field due to a point force in a slit of side  $L$ , i.e.  $L_x = L_z = H = L$ . The point force is located at coordinates  $(0.25L, 0.25L, 0.25L)$ , while its strength is given by  $(F, F, F)$ . The velocity due to this point force will be computed at two target points. The first target point is located at the center of the box  $(0.5L, 0.5L, 0.5L)$ , which is easy to maintain on a mesh point, while the second target point is a randomly chosen point with coordinates  $(0.4312L, 0.3734L, 0.5234L)$ , which is unlikely to be a mesh point. In this test study, we will keep the value of  $\alpha$  fixed at  $\alpha = 80/3L$ , while the value of  $r_{cut} = C/\alpha$  ( $C$  is a constant) and the mean mesh spacing  $\alpha\Delta y_m$  will be varied. Figure (3a) shows the relative error in the  $x$  component of the velocity  $\Delta u/u$  as a function of  $(\alpha\Delta y_m)^{-1}$  for several different values of  $r_{cut}$  for the first target point, while the same is shown for the second target point in Fig. (3b). The data points in these plots were obtained by varying  $N_y$  between 17 and 181, while the solution computed with  $N_y = 225$  and  $r_{cut} = 0.5L$  (i.e.,  $C = 40/3$ ) is taken as the reference for computing the relative error. Focusing first on Fig. (3a), we observe an exponential convergence in the velocity with increasing  $(\alpha\Delta y_m)^{-1}$ , though it eventually levels off at a value depending on the choice of  $r_{cut}$ . For the typical value of  $r_{cut} = 4/\alpha$ , an error of  $O(10^{-6})$  is obtained. We next focus on the velocity convergence at the second target point (Fig. 3b), which is a non-mesh point. For the choice  $r_{cut} = 4/\alpha$ , we again observe an exponential convergence initially with increasing  $(\alpha\Delta y_m)^{-1}$  that eventually levels off at approximately the same value as for the first target point. For higher values of  $r_{cut}$

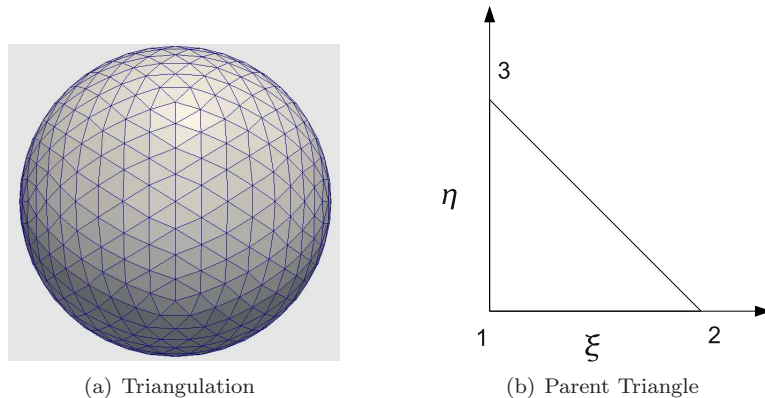


Figure 4: (a) Discretization of a sphere into triangular elements. The number of triangular elements and the number of vertices for the discretization shown in the figure are  $N_{\Delta} = 1280$  and  $N_b = 642$  respectively, (b) A schematic of the parent triangle. Edges 1-2 and 1-3 are of unit length.

( $C = 5$  and  $C = 6$ ), we observe an exponential convergence initially, though a convergence rate scaling as  $(\alpha\Delta y_m)^5$  is observed at higher values of  $(\alpha\Delta y_m)^{-1}$ . The latter convergence rate results from interpolation errors becoming dominant at higher values of  $(\alpha\Delta y_m)^{-1}$ . We also note that an exponential convergence is observed only when the length scale of the global force density is well resolved by the numerical mesh. Since the length scale of the global force density is represented by  $\alpha^{-1}$ , the requirement for an exponential convergence is quantitatively expressed by the condition  $(\alpha\Delta y_m)^{-1} > 1$  (i.e.  $\alpha\Delta y_m < 1$ ). This requirement on the mesh spacing is more easily appreciated if one interprets  $(\alpha\Delta y_m)^{-1}$  as the number of mesh points per unit smearing length represented by  $\alpha^{-1}$ ; therefore the larger is  $(\alpha\Delta y_m)^{-1}$ , the higher is the resolution of the numerical scheme. Based on extensive numerical tests presented in this paper,  $\alpha\Delta y_m = 0.5$  is a recommended value as convergence was usually observed at this resolution.

### 3.3. Surface discretization

Having described the procedure for the fast computation of the velocity and the stress fields associated with a given collection of point forces, we now turn to the numerical solution of the boundary integral equation introduced in Sec. (3.1). In this section, we describe the discretization of the particle's surface into elements along with the basis functions employed over each element. Following this, we describe the numerical implementation of the single and the double layer integrals present in the boundary integral equation. It should be emphasized that accelerated approach described here is not limited to the specific surface discretization used here; this discretization was chosen because it has been used in past works on the dynamics of fluid-filled elastic capsules and drops in flow [11, 31, 51, 43, 64].

In the present work, the surface of a capsule is discretized into triangular elements. Triangulation of a sphere is achieved by mapping the vertices of an icosahedron, which has 12 vertices and 20 triangular faces, to the surface of the inscribed sphere [54]. This procedure will, therefore, give 20 elements on the surface of the sphere. Further refinement is obtained by subdividing each triangular face of the icosahedron recursively

into 4 equal triangular elements, with all the vertices (and consequently the elements) again being mapped to the surface of the inscribed sphere as described above. The number of elements ( $N_\Delta$ ) and the number of vertices ( $N_b$ ) obtained by this procedure can be expressed as  $N_\Delta = 20 \cdot 4^k$  and  $N_b = N_\Delta/2 + 2$ , where  $k$  is the level of refinement ( $k = 0$  corresponds to the original icosahedron). Note that the 12 original vertices of the icosahedron have a coordination number 5, while the remaining vertices have a coordination number of 6. As an example, a sphere subdivided into  $N_\Delta = 1280$  elements with  $N_b = 642$  vertices is shown in Fig. (4(a)).

### 3.3.1. Basis functions over elements

Linear basis functions are used over each element. All computations over a triangular element is performed by mapping to or from the parent triangle [26]. The parent triangle employed in this work is shown in Fig. (4(b)), where  $\xi$  and  $\eta$  denote the natural coordinates. The basis functions associated with the nodes 1, 2, and 3 are respectively given in natural coordinates by

$$\phi_1(\xi, \eta) = 1 - \xi - \eta, \quad (16a)$$

$$\phi_2(\xi, \eta) = \xi, \quad (16b)$$

$$\phi_3(\xi, \eta) = \eta. \quad (16c)$$

As an example, the position vector  $\mathbf{x}$  as a function of natural coordinates  $\mathbf{x}(\xi, \eta)$  is obtained as

$$\mathbf{x}(\xi, \eta) = \phi_1(\xi, \eta) \mathbf{x}_1 + \phi_2(\xi, \eta) \mathbf{x}_2 + \phi_3(\xi, \eta) \mathbf{x}_3, \quad (17)$$

where  $\mathbf{x}_1$ ,  $\mathbf{x}_2$ , and  $\mathbf{x}_3$  are the real space positions of vertices 1, 2, and 3 respectively. The same procedure is employed to obtain the value of any physical variable (e.g. velocity) at coordinates  $(\xi, \eta)$  over the domain of the parent triangle.

### 3.4. Single layer integral

Let the single layer integral over the surface  $S$  be denoted by

$$w_j(\mathbf{z}) = \int_S q_i(\mathbf{x}) G_{ji}(\mathbf{z}, \mathbf{x}) dS(\mathbf{x}), \quad (18)$$

where  $q_i(\mathbf{x})$  is the single layer density, while  $\mathbf{w}(\mathbf{z})$  is assumed to represent the velocity at point  $\mathbf{z}$ . In order to employ GGEM as discussed in Sec. (3.2) to compute the above integral, we write this equation in the form

$$w_j(\mathbf{z}) = \int_S \int_V q_i(\mathbf{x}) \delta(\mathbf{y} - \mathbf{x}) G_{ji}(\mathbf{z}, \mathbf{y}) dS(\mathbf{x}) dV(\mathbf{y}), \quad (19)$$

where  $V$  represents the volume of the domain and  $\delta$  is the three dimensional Dirac delta function. It is easy to see that both the expressions for  $\mathbf{w}(\mathbf{z})$  in Eqs. (18) and (19) are identical. Next, we write the Dirac-delta

function as a sum of the local and the global density introduced in Sec. (3.2); see Eq. (8). Consequently, we have

$$w_j(\mathbf{z}) = \int_S \int_V q_i(\mathbf{x}) (\rho_l(\mathbf{y} - \mathbf{x}) + \rho_g(\mathbf{y} - \mathbf{x})) G_{ji}(\mathbf{z}, \mathbf{y}) dS(\mathbf{x}) dV(\mathbf{y}), \quad (20)$$

Next, we separate the integrals associated with the local and global densities, and write the contribution due to the local density as

$$w_j^l(\mathbf{z}) = \int_S q_i(\mathbf{x}) \left( \int_V \rho_l(\mathbf{y} - \mathbf{x}) G_{ji}(\mathbf{z}, \mathbf{y}) dV(\mathbf{y}) \right) dS(\mathbf{x}). \quad (21)$$

It is easy to see that the above integral can be written as

$$w_j^l(\mathbf{z}) = \int_S q_i(\mathbf{x}) G_{ji}^l(\mathbf{z}, \mathbf{x}) dS(\mathbf{x}), \quad (22)$$

where  $\mathbf{G}^l$  has been defined in Eq. (12). This follows from the fact that the local Green's function  $\mathbf{G}^l(\mathbf{z}, \mathbf{x})$  can also be constructed by the superposition of Green's function  $\mathbf{G}(\mathbf{z}, \mathbf{y})$  weighted by the density  $\rho^l(\mathbf{y} - \mathbf{x})$ , i.e.

$$G_{ji}^l(\mathbf{z}, \mathbf{x}) = \int_V \rho_l(\mathbf{y} - \mathbf{x}) G_{ji}(\mathbf{z}, \mathbf{y}) dV(\mathbf{y}). \quad (23)$$

It is important to emphasize that the domain was assumed to be unbounded in arriving at Eq. (23). This is *always* the case for the local problem as discussed in Sec. (3.2); any error in the boundary condition introduced due to this assumption will be accounted for in the global calculation. Next, consider the contribution from the global density in Eq. (20), which we write as

$$w_j^g(\mathbf{z}) = \int_S \int_V q_i(\mathbf{x}) \rho_g(\mathbf{y} - \mathbf{x}) G_{ji}(\mathbf{z}, \mathbf{y}) dV(\mathbf{y}) dS(\mathbf{x}). \quad (24)$$

It can shown that  $\mathbf{w}^g(\mathbf{z})$  satisfies

$$-\nabla p^{w^g}(\mathbf{z}) + \mu \nabla^2 \mathbf{w}^g(\mathbf{z}) + \mu \mathbf{\Pi}^g(\mathbf{z}) = 0, \quad (25a)$$

$$\nabla \cdot \mathbf{w}^g(\mathbf{z}) = 0, \quad (25b)$$

where the density  $\mathbf{\Pi}^g(\mathbf{z})$  is given by

$$\mathbf{\Pi}^g(\mathbf{z}) = 8\pi \int_S \mathbf{q}(\mathbf{x}) \rho_g(\mathbf{z} - \mathbf{x}) dS(\mathbf{x}). \quad (26)$$

The boundary condition for the global solution comes from the known local solution ( $\mathbf{w}^l(\mathbf{z})$  for  $\mathbf{z}$  at the domain boundary) and the given overall boundary conditions, such that the sum of the local and the global solution satisfies the overall boundary condition; see Sec. (3.2). Having expressed the single layer integral in a form suitable for its computation with the GGEM technique, we next describe its numerical implementation. This includes the numerical solution of the local problem represented by Eq. (22) and the global problem represented by Eq. (25).

### 3.4.1. Local contribution

We first consider the contribution from the local Green's function to the velocity at a given point  $\mathbf{z}$ , which typically is one of the nodes of the elements. We discretize the surface integral in Eq. (22) as

$$w_j^l(\mathbf{z}) = \sum_{k=1}^{N_\Delta N_p} \int_{S_k} q_i(\mathbf{x}) G_{ji}^l(\mathbf{z}, \mathbf{x}) dS(\mathbf{x}), \quad (27)$$

where the summation is over all the triangular elements  $N_\Delta N_p$  present in the system, while  $S_k$  denotes an integral over the element  $k$ . For convenience, all the integrals are performed over the parent triangle. To accomplish this, we write the above equation as

$$w_j^l(\mathbf{z}) = \sum_{k=1}^{N_\Delta N_p} \int_0^1 \int_0^{\xi(\eta)} q_i(\mathbf{x}(\xi, \eta)) G_{ji}^l(\mathbf{z}, \mathbf{x}(\xi, \eta)) \omega d\xi d\eta, \quad (28)$$

where the differential area element  $dS$  has been replaced by its equivalent expression

$$dS = \omega d\xi d\eta = |\mathbf{x}_\xi \times \mathbf{x}_\eta| d\xi d\eta. \quad (29)$$

As noted earlier, the value of any quantity can be obtained at coordinates  $(\xi, \eta)$  by the usual interpolation from the corresponding values at the nodes of the triangle, e.g. see Eq. (17). The double integral in Eq. (28) is evaluated using the product of two one-dimensional Gauss-Legendre quadrature rule (one for  $\xi$  and the other for  $\eta$ ). This proved competitive in terms of computational cost for a given accuracy with Gaussian quadrature rules available for a triangular element [26], perhaps due to the fact that the integrands are not polynomials. In most cases a 4x4 product rule is found to be sufficient for accurate integration over a triangular element. In addition, if the vertex at which the velocity is being computed is a member of the triangular element over which the integration is being performed, then the integral in Eq. (28) over the parent triangle is further transformed to polar coordinates  $(r, \theta)$  [54]. This transformation makes the integrand non-singular and hence ensures sufficient accuracy with the same low order product integration rule discussed above. Lastly, we note that for computing the contribution to velocity at any given point  $\mathbf{z}$  due to the local Green's function, only triangular elements within a distance of  $r_{cut} \sim \alpha^{-1}$  from the point  $\mathbf{z}$  need to be considered (typically,  $r_{cut} = 4/\alpha$ ). This is justified due to the exponentially decaying contribution from the integral over an element at separations larger than  $O(\alpha^{-1})$  from the point of interest. As mentioned in Sec. (3.2.1), the near neighbor list required for the local calculation is generated in  $O(N)$  time via the cell-linked list method [1].

### 3.4.2. Global Contribution

Our goal here is to find  $\mathbf{\Pi}^g(\mathbf{z})$  in Eq. (25), for which we need to compute the integral in Eq. (26). We begin by discretizing the integral in Eq. (26) and write it as

$$\mathbf{\Pi}^g(\mathbf{z}) = \sum_{k=1}^{N_{\Delta}N_p} \int_{S_k} q_i(\mathbf{x}) \rho_g(\mathbf{z} - \mathbf{x}) dS(\mathbf{x}). \quad (30)$$

The above integral can be evaluated with any desired quadrature rule, though, due to the smoothly varying nature of the integrand a simple trapezoidal rule proves sufficient. Note that the trapezoidal integration rule essentially reassigns the contribution from the surface of the triangular element to its three vertices in equal proportions. Consider first the integral over an element  $S_k$  in Eq. (30), which as per the trapezoidal rule is expressed as a sum of contributions from its three vertices as

$$[\mathbf{\Pi}_i^g(\mathbf{z})]_{S_k} = \sum_{p=1}^3 \left( \frac{A_k q_i(\mathbf{x}^{k_p})}{3} \right) \rho_g(\mathbf{z} - \mathbf{x}^{k_p}), \quad (31)$$

where  $A_k$  is the area of the triangular element  $S_k$ ,  $p$  denotes the vertex number of the given element  $k$ ,  $\mathbf{x}^{k_p}$  denotes the coordinate of the  $p^{th}$  vertex of the triangular element  $k$ , and  $[\mathbf{\Pi}^g(\mathbf{z})]_{S_k}$  denotes the density at  $\mathbf{z}$  due to the integration over the element  $S_k$  only. The term in the parenthesis in Eq. (31) can be considered as the strength of the global density at the node  $\mathbf{x}^{k_p}$  due to the element  $k$ ; by summing it over all the elements  $k$  to which a given node belongs (let us say that this node is *globally* represented by  $\mathbf{x}^b$ ), one obtains the total strength of the global density at this node, say  $\mathbf{q}^{\mathbf{x}^b}$ . The overall density at a point  $\mathbf{z}$  is then obtained by adding contributions from all the nodes present in the system,

$$\mathbf{\Pi}_i^g(\mathbf{z}) = \sum_{p=1}^{N_b} q_i^{\mathbf{x}^b} \rho_g(\mathbf{z} - \mathbf{x}^b), \quad (32)$$

where  $N_b$  is the total number of nodes in the system. We also note that due to the exponentially decaying nature of  $\rho_g(\mathbf{z} - \mathbf{x}^b)$  as a function of distance from  $\mathbf{x}^b$ , we consider only those nodes for computing the density at a point  $\mathbf{z}$  which are within a distance  $r_{cut} \sim \alpha^{-1}$  from it. Once  $\mathbf{\Pi}^g(\mathbf{z})$  is evaluated, we solve the set of equations in (25) using the procedure described in detail in Sec. (3.2). This gives us  $\mathbf{w}^g(\mathbf{z})$  at the mesh points. The velocity  $\mathbf{w}^g(\mathbf{z})$  at any point not on the mesh is obtained using 4<sup>th</sup> order Lagrange interpolation. Once  $\mathbf{w}^g(\mathbf{z})$  is known, the overall single layer integral  $\mathbf{w}(\mathbf{z})$  is obtained as:

$$\mathbf{w}(\mathbf{z}) = \mathbf{w}^l(\mathbf{z}) + \mathbf{w}^g(\mathbf{z}). \quad (33)$$

### 3.5. Double layer integral

We now describe the evaluation of the double layer integral. We denote the double layer integral over a surface  $S$  (similar to that in Eq. 3) by

$$v_j(\mathbf{z}) = n_k(\mathbf{z}) \int_S q_i(\mathbf{x}) T_{jik}(\mathbf{z}, \mathbf{x}) dS(\mathbf{x}). \quad (34)$$

If we define a stress tensor  $\boldsymbol{\sigma}(\mathbf{z})$  as (note that one needs to multiply it by  $\mu$  to get units of stress)

$$\sigma_{jk}(\mathbf{z}) = \int_S q_i(\mathbf{x}) T_{jik}(\mathbf{z}, \mathbf{x}) dS(\mathbf{x}), \quad (35)$$

then we have the following relationship between  $\mathbf{v}(\mathbf{z})$  and  $\boldsymbol{\sigma}(\mathbf{z})$ :

$$v_j(\mathbf{z}) = n_k(\mathbf{z}) \sigma_{jk}(\mathbf{z}). \quad (36)$$

The motivation for introducing the stress field  $\boldsymbol{\sigma}(\mathbf{z})$  in Eq. (35) should be clear now, as it is the stress field associated with the following velocity field

$$w_j(\mathbf{z}) = \int_S q_i(\mathbf{x}) G_{ji}(\mathbf{z}, \mathbf{x}) dS(\mathbf{x}). \quad (37)$$

As described in the previous section (3.4), we write the above velocity field as the sum of a local  $\mathbf{w}^l(\mathbf{z})$  and global  $\mathbf{w}^g(\mathbf{z})$  velocity fields, and denote the corresponding stress fields by  $\boldsymbol{\sigma}^l(\mathbf{z})$  and  $\boldsymbol{\sigma}^g(\mathbf{z})$  respectively. Using (36), we obtain the corresponding local and global contributions to the double layer integral as

$$v_j^l(\mathbf{z}) = n_k(\mathbf{z}) \sigma_{jk}^l(\mathbf{z}), \quad (38a)$$

$$v_j^g(\mathbf{z}) = n_k(\mathbf{z}) \sigma_{jk}^g(\mathbf{z}). \quad (38b)$$

We describe the computation of the global contribution to the double layer integral first, as it is a straightforward extension of the procedure presented in Sec. (3.4). This will be followed by a discussion of the procedure for computing the local contribution to the double layer integral.

#### 3.5.1. Global contribution

Here we describe the procedure to compute the global contribution to the double layer integral. Consider the global velocity field  $\mathbf{w}^g(\mathbf{z})$  and the pressure field  $\mathbf{p}^{w^g}(\mathbf{z})$  associated with the global force density  $\boldsymbol{\Pi}^g(\mathbf{z})$ ; see Eq. (25). The procedure to compute the velocity and pressure field for this *global* distribution of density has been discussed in detail in Sec. (3.4). Once these are known, one can obtain the stress field  $\boldsymbol{\sigma}^g(\mathbf{z})$  from the usual Newtonian constitutive equation as

$$\sigma_{jk}^g(\mathbf{z}) = -\frac{p^{w^g}(\mathbf{z})}{\mu} \delta_{jk} + \left( \frac{\partial w_j^g(\mathbf{z})}{\partial x_k} + \frac{\partial w_k^g(\mathbf{z})}{\partial x_j} \right). \quad (39)$$

As was mentioned in Sec. (3.2), the differentiations required in the above expression are performed in the transform space [6, 49]; consequently, the stress field is known with spectral accuracy at the mesh points. Once the stress tensor is obtained at the mesh points, the stress at the nodes of the elements are obtained using 4<sup>th</sup> order Lagrange interpolation. Lastly,  $\mathbf{v}^g(\mathbf{z})$  is obtained from Eq. (38b).

### 3.5.2. Local contribution

Consider the velocity field due to the local density, which is written as

$$w^l(\mathbf{z}) = \int_S q_i(\mathbf{x}) G_{ji}^l(\mathbf{z}, \mathbf{x}) dS(\mathbf{x}). \quad (40)$$

It is trivial to show that the stress field associated with the above velocity field is given by the following

$$\sigma_{jk}^l(\mathbf{z}) = \int_S q_i(\mathbf{x}) T_{jik}^l(\mathbf{z}, \mathbf{x}) dS(\mathbf{x}), \quad (41)$$

and consequently the local contribution to the double layer integral is given by

$$v_j^l(\mathbf{z}) = n_k(\mathbf{z}) \int_S q_i(\mathbf{x}) T_{jik}^l(\mathbf{z}, \mathbf{x}) dS(\mathbf{x}). \quad (42)$$

The above integral is discretized in the same fashion as in Sec. (3.4), and is written as a sum of integrals over the triangular elements. Again, as in Sec. (3.4.1), all the integrals are performed over the parent triangle as follows

$$v_j^l(\mathbf{z}) = n_k(\mathbf{z}) \sum_{k=1}^{N_\Delta N_p} \int_0^1 \int_0^{\xi(\eta)} q_i(\mathbf{x}(\xi, \eta)) T_{jik}^l(\mathbf{z}, \mathbf{x}(\xi, \eta)) \omega d\xi d\eta. \quad (43)$$

The integral in the above equation is performed with the product of two one dimensional Gauss-Legendre quadrature rule; see Sec (3.4.1) for details. In addition, when the vertex at  $\mathbf{z}$  is a member of the element over which integration is performed, the integrand is singular and requires special treatment. At this point it is worth noting that the double layer integrand has the same  $1/\hat{r}$  singularity as the single layer integral [47], as  $\hat{\mathbf{x}} \cdot \mathbf{n}(\mathbf{x}_0) \approx \hat{r}^2$  for small  $\hat{r}$ . So in principle one may employ the polar coordinate transformation to regularize the singular double layer integral. In practice, because we employ flat elements, the condition  $\hat{\mathbf{x}} \cdot \mathbf{n}(\mathbf{x}_0) \approx \hat{r}^2$  is not valid. Note that the normal vector at any given vertex is taken as the area averaged normal vector of triangles to which it belongs, from which it follows that the numerical double layer has a  $1/\hat{r}^2$  singularity. This stronger singularity can be avoided by employing surface elements that yields a continuously varying normal vector such as splines [36].

In the literature, desingularization of the double layer integral is usually achieved by singularity subtraction [50]. This desingularization scheme is also applicable for the current formulation (34), though this procedure will require 9 times the computational effort of performing the double layer integral itself; we omit the details here. We therefore look elsewhere for more computationally efficient schemes for performing the singular part of the double layer integral. The first point to note is that the singularity in the stress tensor

$\mathbf{T}(\mathbf{z}, \mathbf{x})$  is contained entirely in its local part  $\mathbf{T}^l(\mathbf{z}, \mathbf{x})$ . Moreover, desingularization is necessary only when the target point  $\mathbf{z}$  is one of the vertices of the element over which integration is being performed. If this is the case, we proceed by replacing the normal vector  $\mathbf{n}(\mathbf{z})$  outside the integral in Eq. (43) by a vector  $\tilde{\mathbf{n}}(\mathbf{x})$  inside the integral, which leads to the following expression for the integral over the current element  $k$ :

$$[v_j^l(\mathbf{z})]_{S_k} = \int_{S_k} q_i(\mathbf{x}) T_{jik}^l(\mathbf{z}, \mathbf{x}) \tilde{n}_k(\mathbf{x}) dS(\mathbf{x}). \quad (44)$$

The vector  $\tilde{\mathbf{n}}(\mathbf{x})$  at any point  $\mathbf{x}(\xi, \eta)$  on the element is defined as per the following equation:

$$\tilde{\mathbf{n}}(\mathbf{x}) = \mathbf{n}_\Delta \phi_1(\xi, \eta) + \mathbf{n}(\mathbf{z}) \phi_2(\xi, \eta) + \mathbf{n}(\mathbf{z}) \phi_3(\xi, \eta), \quad (45)$$

where  $\mathbf{n}_\Delta$  refers to the normal vector of the current triangular element. In writing the above equation, we have assumed that the target point  $\mathbf{z}$  is mapped to the vertex labeled 1 of the parent triangle; see Fig. 4(b). It is immediately clear from Eq. (45) that  $\tilde{\mathbf{n}}(\mathbf{x})$  will take the value  $\mathbf{n}_\Delta$  when the source point coincides with the target point (i.e., when  $\mathbf{x} = \mathbf{z}$ ), while it will tend to  $\mathbf{n}(\mathbf{z})$  as the source point  $\mathbf{x}$  moves away from the target point  $\mathbf{z}$  over the current element. Now, if we substitute the expression of  $\mathbf{T}^l$  from Eq. (12) into Eq. (44), one immediately sees that the singular parts of the integrand tends to zero as the source point approaches the target point since  $\hat{\mathbf{x}} \cdot \mathbf{n}_\Delta = 0$ . This is due to the fact that elements are flat and  $\hat{\mathbf{x}}$  lies in the plane of the element, while  $\mathbf{n}_\Delta$  is normal to the element. In order to estimate the error introduced due to this approximation, one can show by simple Taylor series expansion that  $\|\tilde{\mathbf{n}}(\mathbf{x}) - \mathbf{n}(\mathbf{z})\| \sim \|\nabla \mathbf{n}(\mathbf{z})\| h_s$ , where  $h_s$  is the characteristic surface mesh spacing scaling as  $N_\Delta^{-1/2}$ . In addition, since this approximation is applied only when the target point is a member of the triangle over which the integration is being performed, the previous error gets multiplied by the area of the triangle which is  $O(N_\Delta^{-1})$ . Therefore, we estimate the error introduced in the solution due to this approximation as  $O(N_\Delta^{-3/2})$ . This completes the evaluation of the local contribution to the double layer integral. The total double layer integral is then obtained as the sum of the local and the global parts as:

$$v_j(\mathbf{z}) = v_j^l(\mathbf{z}) + v_j^g(\mathbf{z}). \quad (46)$$

#### 4. Membrane Mechanics: Hydrodynamic traction jump

The solution of the boundary integral equation (3) requires the knowledge of the hydrodynamic traction jump across the interface  $\Delta \mathbf{f}$ . This jump in traction is obtained from the membrane equilibrium condition as discussed next. Consider first a patch of element on the membrane's surface as shown in Fig. (5a). The forces acting on this patch are the hydrodynamic stresses on the inner and the outer surface and the membrane tension at the boundary denoted by contour  $C$ . Now, let the membrane tension tensor be given

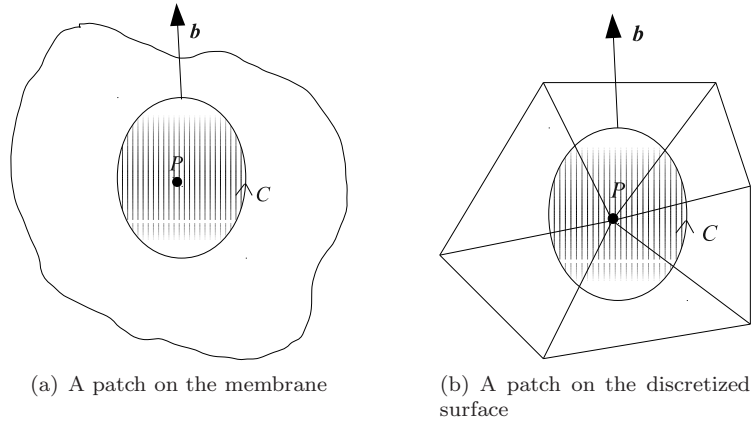


Figure 5: Defining the contour  $C$  enclosing an area (hatched) containing the point of interest  $P$ .  $\mathbf{b}$  is the in-plane normal to the contour  $C$ .

by  $\boldsymbol{\tau}$ , then the force balance on the membrane patch is given by

$$\int_{S_C} \Delta \mathbf{f} dS + \int_C \mathbf{b} \cdot \boldsymbol{\tau} dl = 0, \quad (47)$$

where  $S_C$  denotes the area enclosed by the contour  $C$ . Using the divergence theorem, one can convert to contour integral to a surface integral, which in the limit of infinitesimal area yields

$$\Delta \mathbf{f} = -\nabla_s \cdot \boldsymbol{\tau}, \quad (48)$$

where  $\nabla_s$  is the surface divergence operator [3]. The above equation (48) has been directly employed in several boundary integral implementations to obtain the traction jump  $\Delta \mathbf{f}$ ; see e.g. Lac et al. [35]. For flat elements as in this work, we note that  $\boldsymbol{\tau}$  is constant over each element such that its surface divergence is identically zero, though there is a jump in its value across elements and consequently the contour integral in the Eq. (47) is generally expected to be non-zero. The Contour integral can therefore be used to obtain the traction jump as [54]

$$\Delta \mathbf{f} = -\frac{1}{A_C} \int_C \mathbf{b} \cdot \boldsymbol{\tau} dl, \quad (49)$$

where the  $A_C$  is the area enclosed by the contour  $C$ ; Fig. (5b) shows an example of the contour for the discretized surface. To proceed with our implementation, we first interpret the contour integral on the right of (49) as the reaction force on a given node obtained under the condition that the entire elastic energy stored in the particle membrane has been reassigned to the vertices of the discretized triangular elements. We then use the principal of virtual work as presented by Charrier et al. [8] to compute the reaction force at the vertices. Once the total reaction force  $\mathbf{F}_p$  at a given vertex  $P$  is known, we obtain the traction discontinuity at that vertex as

$$\Delta \mathbf{f}_p = -\frac{\mathbf{F}_p}{A_p} \quad (50)$$

where  $A_p$  is area assigned to the vertex, which is essentially the area enclosed by a hypothetical contour around the vertex  $P$ ; see Fig. (5b). We call the contour hypothetical as we never explicitly define it here. For the area assignment to the vertex, we use a very simple rule where each vertex of the triangular element is assigned a third of the triangular element's area. Therefore the total area  $A_p$  is obtained as  $(1/3)$  of the total area of the triangular elements of which the given vertex  $P$  is a member. We believe the method outlined here is substantially simpler to implement than employing the contour integral explicitly. In the remainder of this section, we outline the procedure employed for computing the reaction force at the vertices of the triangular elements.

We begin by introducing the formalism for describing the kinematics of the membrane deformation. This formalism is mostly clearly presented for deformations in a plane, which for the moment is taken to be the  $xy$  plane. Let  $(x, y)$  and  $(X, Y)$  denote respectively the undeformed and deformed coordinates of a material point, with respect to a fixed set of Cartesian axes. If  $u$  and  $v$  denote the displacements of the material point in  $x$  and  $y$  directions respectively, then

$$\begin{aligned} X &= x + u, \\ Y &= y + v. \end{aligned} \tag{51}$$

The relationship between an infinitesimal line segment before and after the deformation can be expressed as

$$\begin{bmatrix} dX \\ dY \end{bmatrix} = \begin{bmatrix} 1 + \partial u / \partial x & \partial u / \partial y \\ \partial v / \partial x & 1 + \partial v / \partial y \end{bmatrix} \begin{bmatrix} dx \\ dy \end{bmatrix}, \tag{52}$$

or compactly as

$$d\mathbf{X} = \mathbf{F} \cdot d\mathbf{x}. \tag{53}$$

where  $\mathbf{F}$  is the deformation gradient tensor. The square of the distance between the two neighboring points after deformation is given by

$$\begin{aligned} dS^2 &= d\mathbf{X} \cdot d\mathbf{X} = d\mathbf{x} \cdot \mathbf{G} \cdot d\mathbf{x}, \\ \mathbf{G} &= \mathbf{F}^T \cdot \mathbf{F}, \end{aligned} \tag{54}$$

where  $\mathbf{G}$  is a symmetric positive definite matrix. We denote the eigenvalues of the  $\mathbf{G}$  by  $\lambda_1^2$  and  $\lambda_2^2$ , such that  $\lambda_1$  and  $\lambda_2$  are the principal stretch ratios. For a thin membrane that displays no resistance to bending, the strain energy density  $W$  of the membrane is a function of  $\lambda_1$  and  $\lambda_2$ . Here we consider the capsule to be an infinitely thin neo-Hookean membrane, for which the strain energy density is defined as [4]

$$W_{\text{NH}} = \frac{G}{2} \left[ \lambda_1^2 + \lambda_2^2 + \frac{1}{\lambda_1^2 \lambda_2^2} - 3 \right]. \tag{55}$$

Here  $G$  is the two-dimensional shear modulus for the membrane, having units of force per unit length. To compute the reaction force at the nodes, we adopt the finite element approach of Charrier et al. [8]. Only the briefest account will be given here; for details the reader is referred to the original reference. In the

approach of Charrier et al. [8], the membrane is discretized into flat triangular elements such that the strain is uniform over an element. Moreover, it is assumed that an element remains flat even after deformation. The forces at the nodes are then determined from the knowledge of the displacement of the vertices of the element with respect to the undeformed element followed by the application of the principle of virtual work, such that the computed forces and the known displacements are consistent with the strain energy stored in the element. For an arbitrarily oriented element, rigid body rotations and translations can be defined to make the deformed and undeformed state in the same plane. Note that the rigid body rotations and translations have no effect on the strain energy and consequently the forces. The forces are then computed using the coplanar formalism discussed above. Finally, these forces are transformed back to the frame of reference in the deformed state by applying the inverse transformation. The total reaction force at a node is obtained as a sum of reaction forces at that node due to contributions from all the triangular elements of which it is a member. Once the reaction force at any given node is known, the hydrodynamic traction discontinuity at that node is obtained from Eq. (50) as detailed earlier.

## 5. Solution procedure and parameters

In this section we describe solution methods and parameters for the equations resulting from the formulation just presented.

The heart of the computation is the determination of the fluid velocity at the element nodes using equations (2) and (3). To compute the velocity from Eq. (2), we first need to compute the single layer density  $\mathbf{q}(\mathbf{x})$ . This is obtained from the solution of the integral equation (3). Upon discretization of the double layer integral in Eq. (3), which was discussed in Sec. (3.5), we obtain a linear coupled system of equations for  $\mathbf{q}^b$ , where  $\mathbf{q}^b$  is a vector of length  $3N_b$  denoting the value of  $\mathbf{q}(\mathbf{x})$  at the element nodes;  $N_b$  is the number of element nodes in the system. We express this linear system of equations as

$$\left(\mathbf{I} + \frac{\boldsymbol{\kappa}}{4\pi} \cdot \mathbf{D}^I\right) \cdot \mathbf{q}^b = \mathbf{b}, \quad (56)$$

where  $\boldsymbol{\kappa}$  is a diagonal matrix of size  $3N_b \times 3N_b$  denoting the value of  $\kappa_m$  in Eq. (3) at each element node,  $\mathbf{D}^I$  denotes the discretized double layer operator of size  $3N_b \times 3N_b$ , while  $\mathbf{b}$  is a  $3N_b$  vector denoting the known right hand side of Eq. (3) at the element nodes. The above system of equations is solved iteratively using the GMRES algorithm [55]. An important benefit of this iterative procedure is that the matrix in the parenthesis above is never explicitly computed; at each iteration step only the product of the above matrix with a known vector generated by the algorithm is to be computed. The procedure to compute this matrix vector product is similar to computing  $\mathbf{v}(\mathbf{z})$  in Sec. (3.5) (see Eq. 34) at the element nodes for a known  $\mathbf{q}^b$ . We take the initial guess for  $\mathbf{q}^b$  either from the previous time step, or from the previous stage if a multistage method is employed as is the case here. This leads to a substantial savings in the number

of iterations required for convergence. Iterations were terminated when the  $L_2$  norm of the current residual vector  $\mathbf{S}$  relative to the norm of the right hand side  $\mathbf{b}$  was less than  $10^{-4}$ ; the residual vector  $\mathbf{S}$  is defined as

$$\mathbf{S} = (\mathbf{I} + \frac{\boldsymbol{\kappa}}{4\pi} \cdot \mathbf{D}^T) \cdot \mathbf{q}^b - \mathbf{b}. \quad (57)$$

In addition to the convergence in the residual vector  $\mathbf{S}$ , which is obtained naturally as part of the iterative procedure, it is also important to investigate the convergence in the solution; the error in solution denoted by vector  $\mathbf{S}_q$  is defined as

$$\mathbf{S}_q = \mathbf{q}^b - \mathbf{q}_{ex}^b \quad (58)$$

where we have defined the “exact” solution as  $\mathbf{q}_{ex}^b$ , which can be obtained by solving the above system of equations to a very small tolerance, e.g.  $10^{-10}$ . The above tolerance of  $10^{-4}$  for the residual vector relative to the norm of the right hand side leads to an error of the same order for the error vector relative to the exact solution for well conditioned systems. This implies an accuracy of 0.01% for most cases. Even for the worst cases in the present work, the relative error in the solution was always less than 0.1%. In most cases convergence was achieved in less than 5 iterations; see Sec. (7) for some examples. For systems with high viscosity contrast and/or with large number of particles, the matrix may become ill-conditioned and a preconditioner may become necessary. In the present study, no preconditioner was employed, though multigrid preconditioners for Stokes flow may be useful [12, 56].

The iterative procedure described above gives the  $\mathbf{q}^b$  vector at the element nodes. These are subsequently substituted in Eq. (2) to compute the corresponding velocity at the element nodes; the numerical procedure described in Sec. (3.4) is employed to compute this single layer integral. We denote the velocity thus computed at the element nodes by a  $3N_b$  vector  $\mathbf{u}^b$ , which is used to evolve the position of element nodes  $\mathbf{x}^b$  as per the equation

$$\frac{d\mathbf{x}^b}{dt} = \mathbf{u}^b. \quad (59)$$

The time integration in the above equation is performed via the second order midpoint method, which belongs to the family of explicit Runge-Kutta integrators [37]. The time step  $\Delta t$  employed in this work was set adaptively using the rule [43, 53]:

$$\dot{\gamma}\Delta t = 0.5 Ca h_s^m/a, \quad (60)$$

where  $h_s^m$  is the minimum node-to-node separation in the system (which does not have to be for two points on the same particle),  $a$  quantifies the length scale of the particle such as the radius for a spherical particle,  $\dot{\gamma}$  is the shear rate, while  $Ca$  is the capillary number, expressing the ratio of viscous and interfacial stresses (for a spherical capsule with radius  $a$  and shear modulus  $G$ , the capillary number is defined as  $Ca = \mu\dot{\gamma}a/G$ ). This rule gave a stable evolution with time; a time step twice this value led to an instability in some simulations presented later, while a time step half this size gave nearly indistinguishable result. The volume of the

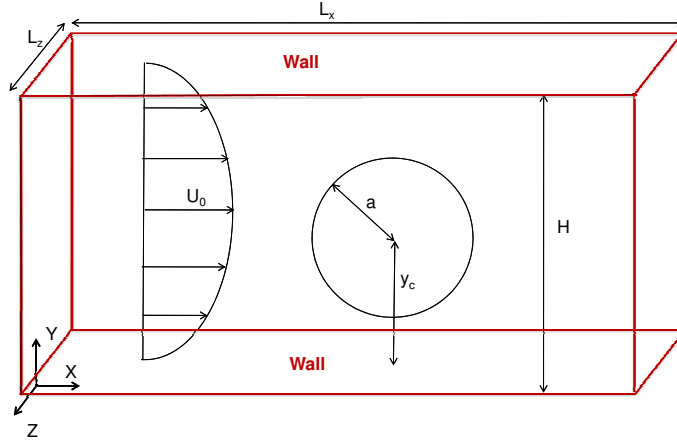


Figure 6: Schematic of the slit geometry for the test problems in Secs. (6.1) and (6.2). A single sphere, either a rigid particle or a drop, is placed in a slit geometry with the channel height being  $H$ . The radius of the sphere is  $a$ , while its center is at  $y_c$ . A pressure driven flow is considered with  $U_0$  being the centerline velocity. The confinement ratio is  $2a/H$ . Periodic boundary conditions are employed in  $x$  and  $z$  directions, with periodicity being  $L_x$  and  $L_z$  respectively.

particle was found to be well conserved with time. For example, for a capsule with  $\lambda = 5$  in shear flow at  $Ca = 0.6$ , the volume changed by an average of  $10^{-4}$  of its original value over a unit strain. In the present work, a volume correction was performed only when the volume of the particle deviated by more than  $10^{-4}$  of its original value; the procedure employed for this correction is described in [16].

Finally, we consider parameters related to the numerical solution procedure. Many of these have already been introduced earlier, and are repeated here for completeness. The first parameter is  $N_\Delta$ , which refers to the number of triangular elements employed to discretize the surface of each of the  $N_p$  particles in the system; the number of element nodes per particle is denoted by  $N_b$ . Next, there are several parameters associated with the GGEM methodology described in Sec. (3.2). First is the length scale  $\alpha^{-1}$  associated with the quasi-Gaussian global density. The local solution as well as the assignment of the global force density to mesh points is truncated beyond a distance of  $r_{cut} = 4/\alpha$  from the origin of the singularity. The solution of the global problem (Sec. 3.2) requires one to define a three dimensional mesh with  $N_x$ ,  $N_y$ , and  $N_z$  mesh points in  $x$ ,  $y$  and  $z$  directions respectively. This gives a mean mesh spacing in the three directions as  $\Delta x_m = L_x/N_x$ ,  $\Delta y_m = H/(N_y - 1)$  and  $\Delta z_m = L_z/N_z$ ; all three mean mesh spacings are kept equal unless otherwise mentioned. An important parameter denoting the resolution of the GGEM methodology is  $\alpha\Delta y_m$ , with the resolution and hence the accuracy of the method increasing with decreasing  $\alpha\Delta y_m$ . As a rule of thumb, we require  $\alpha\Delta y_m < 1$ ; see Sec. (3.2.3) for details. Choices of above parameters are specified below in the descriptions of the test problems.

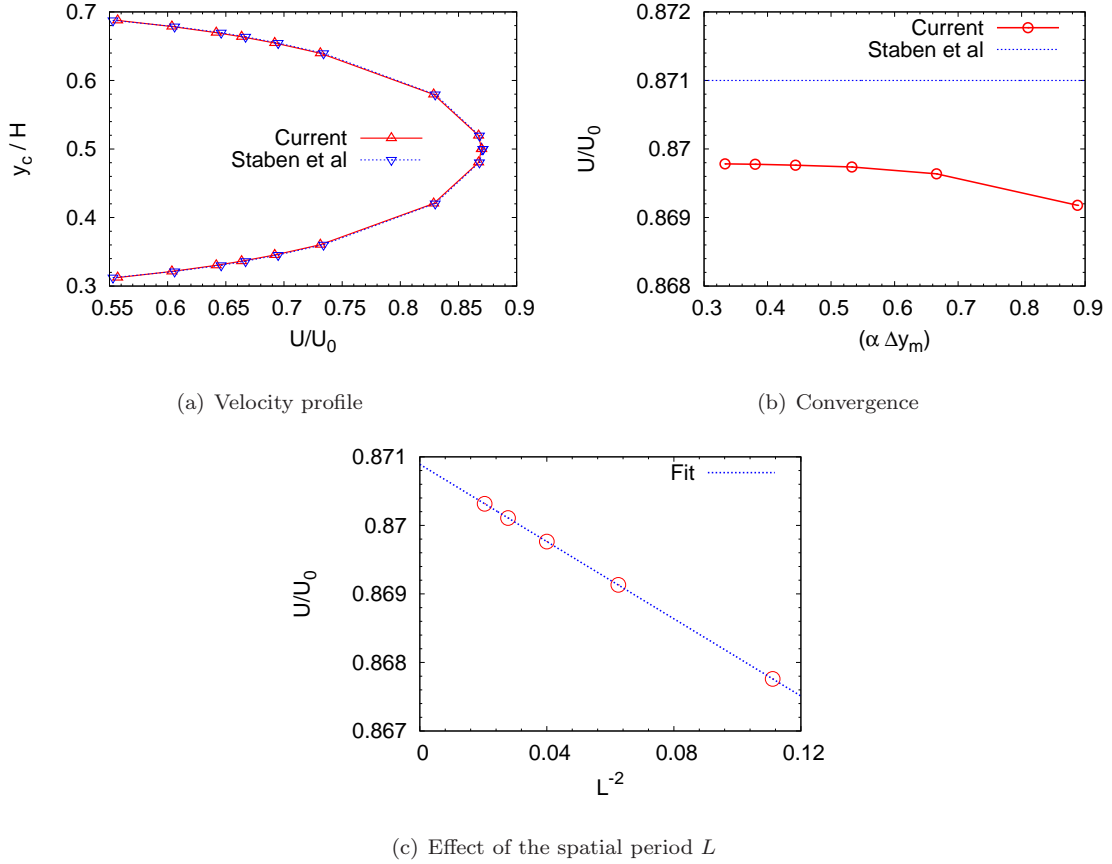


Figure 7: Rigid particle in a slit: (a) Comparison of the translational velocity of a rigid sphere in a slit geometry with results of Staben et al. [58]. The confinement ratio of the particle was  $2a/H = 0.6$ . The horizontal axis gives the velocity of the particle non-dimensionalized by the centerline velocity of the undisturbed fluid, while the vertical axis gives the location of the center of the sphere along the gradient direction non-dimensionalized by the height of the channel. Walls are present at  $y = 0$  and  $y = H$ . Simulation parameters were:  $N_y = 61$ ,  $\alpha\Delta y_m = 0.44$ ,  $N_\Delta = 5120$ ,  $L_x = L_z = 5H$ , and  $\Delta x_m = \Delta y_m = \Delta z_m$ ; see text for details. (b) Convergence of the velocity for  $y_c/H = 0.5$  with  $\alpha\Delta y_m$ . For this calculation  $r_{cut} = 0.5a$  is kept fixed, while  $N_y$  is varied between 17 and 81. (c) Effect of the spatial period  $L = L_x = L_z$  on the translational velocity of a particle with  $y_c/H = 0.5$ . Also shown is a linear fit to the data in the plot. All simulation parameters in (c) were the same as in (a) above except for  $L_x$  and  $L_z$  which were varied.

## 6. Numerical Results: Validation

### 6.1. Single layer validation: Rigid particle in a slit

As a validation of the single layer integral implementation, we consider a rigid sphere between two parallel walls and subject it to a pressure driven flow with a centerline velocity  $U_0$  as shown in Fig. (6). For a rigid particle, the velocity at a point  $\mathbf{x}_0$  on the surface satisfies the following integral equation [30]

$$u_j(\mathbf{x}_0) = u_j^\infty(\mathbf{x}_0) - \frac{1}{8\pi\mu} \int_S f_i(\mathbf{x}) G_{ji}(\mathbf{x}_0, \mathbf{x}) dS(\mathbf{x}), \quad (61)$$

where  $\mathbf{f}$  is the traction on the external surface of the sphere due to the stresses in the fluid. The velocity at the surface of the particle  $\mathbf{u}(\mathbf{x}_0)$  in the above equation can be written as

$$\mathbf{u}(\mathbf{x}_0) = \mathbf{U} + \boldsymbol{\Omega} \times (\mathbf{x}_0 - \mathbf{x}_c), \quad (62)$$

where  $\mathbf{U}$  and  $\boldsymbol{\Omega}$  represent the translational and rotational velocities of the particle, and  $\mathbf{x}_c$  denotes the center of the sphere. Here we take the particle to be force and torque free and our goal is to compute the velocity and angular velocity of the particle. For this particular problem, the surface of the sphere was discretized into  $N_\Delta = 5120$  triangular elements with  $N_b = 2562$  vertices. The unknowns in the discretized system are  $3N_b$  tractions at element vertices, along with  $\mathbf{U}$  and  $\boldsymbol{\Omega}$ . The force and torque free condition along with the discretization of Eq. (61) gives  $3N_b + 6$  equations, which were solved iteratively using the GMRES algorithm [55].

Translational and rotational velocities of a rigid sphere between two infinite parallel walls have been reported previously by Staben et al. [58]. Here, we compare the translational velocity obtained in the present work with their results for a fixed confinement ratio of  $2a/H = 0.6$  and for various positions of the sphere's center along the channel height  $y_c$ . This comparison is shown in Fig. (7a), where the velocity of the particle has been non-dimensionalized by the velocity of the undisturbed flow at the centerline  $U_0$ , while the height of the sphere's center has been non-dimensionalized by the channel height  $H$ . Very good agreement between the two results was observed, with the discrepancy typically being less than 0.8%; the source of the slight discrepancy is discussed below. The GGEM parameters employed in the above calculation were:  $N_y = 61$  and  $r_{cut} = 0.5a$ , which gives  $\alpha\Delta y_m = 0.44$ ; note that  $r_{cut} = 4/\alpha$ . The mean mesh spacing was equal in all three directions ( $\Delta x_m = \Delta y_m = \Delta z_m$ ), and the spatial period in both  $x$  and  $z$  directions were set to five times the wall spacing:  $L_x = L_z = 5H$ . Convergence of the particle velocity with respect to  $\alpha\Delta y_m$  is demonstrated next in Fig. (7b) for a particle placed at the centerline, i.e.  $y_c/H = 0.5$ . For this calculation  $r_{cut} = 0.5a$  was held constant, while  $\alpha\Delta y_m$  was varied by varying  $N_y$  between 17 and 81 ( $N_x$  and  $N_z$  varied between 80 and 340). As could be seen in the figure, the velocity of particle reaches its converged value for  $\alpha\Delta y_m < 0.5$  and shows very little variation with any further increase in mesh resolution. Also shown in this plot is the result of Staben et al. [58] which reveals that the velocity obtained in this work converges to a slightly lower value than the previous reference. The source of this discrepancy can be traced to the periodic boundary conditions employed in  $x$  and  $z$  directions in the present work; Staben et al. [58] used an unbounded domain in these directions. In the present case, we can easily estimate the result for an infinite box by observing its trend in a series of simulations with varying spatial period  $L$  ( $L = L_x = L_z$ ). This procedure is commonly used in triply periodic simulations to remove the effects of the periodic boundary conditions; see, e.g. [34]. In this particular example, we numerically find that the periodic image effects decay as  $L^{-2}$  as shown in Fig. (7c), where we have plotted the translational velocity of the particle against

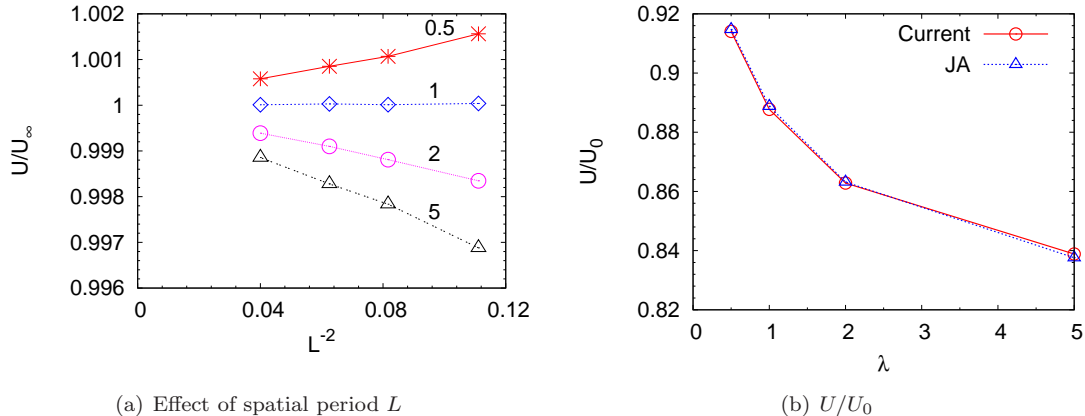


Figure 8: Volume averaged translational velocity of a spherical drop in a slit. The confinement ratio of the drop is  $2a/H = 0.6$ , while its center is at  $y_c/H = 0.4$ . The simulation parameters are:  $N_y = 61$ ,  $\alpha\Delta y_m = 0.44$ ,  $N_\Delta = 5120$ , and  $\Delta x_m = \Delta y_m = \Delta z_m$ . (a) Effect of the spatial period  $L = L_x = L_z$  on the drop's velocity for different viscosity ratios  $\lambda$ . Note the velocity has been non-dimensionalized by  $U_\infty$ , which is the estimated velocity of the drop as  $L \rightarrow \infty$ . This is obtained by fitting a straight line to the data which have not been non-dimensionalized by  $U_\infty$ ; the y-intercept of this fit gives  $U_\infty$ . (b) Comparison of the volume averaged translational velocity of a drop as a function of viscosity ratio with the results of Janssen and Anderson [28] (JA). The velocity in the current work corresponds to  $U_\infty$  in (a) above.

$L^{-2}$ . The y-intercept of the linear fit through the data points in the previous plot then gives an estimate of the particle velocity in an infinite slit. This value comes out to be  $0.871U_0$  (rounded to three significant digits), which is exactly equal to the value reported by Staben et al. [58]. Recall that their boundary integral formulation is based on the slit Green's function of Liron and Mochon [42]; the agreement of our results with those of Staben et al. [58] thus implicitly validates our Green's function implementation for a slit with respect to the Green's function provided by Liron and Mochon [42]. In addition to the periodic image effects, a slight discrepancy between our results and those of Staben et al. [58] can also be expected in cases where the particle-wall separation is very small. In such problems, a large lubrication pressure can develop in the region around the small gap [30, 33]. To obtain accurate solutions in this case, the surface discretization of the particle near the small gap must be adaptively refined as was done by Staben et al. [58]. No fundamental changes to the present formalism would be required to implement adaptive refinement.

### 6.2. Single and double layer validation: A Drop in a slit

Having validated the single layer integral, we next move on to the validation of the double layer integral. For this, we consider the same geometry and bulk flow as in the above test case (Fig. 6), but now consider a spherical drop instead of a rigid sphere. The motion of the drop can be obtained by first solving Eq. (3) for  $\mathbf{q}(\mathbf{x})$ , which upon substitution in Eq. (2) gives the velocity on the surface of the drop. We first point out that for a spherical drop, the interfacial traction jump  $\Delta\mathbf{f}$  is inconsequential. This is due to the fact that  $\Delta\mathbf{f}$  is uniform in strength and acts radially everywhere, which when combined with the incompressibility of the fluid implies zero velocity contribution from this term. Once the velocity at the surface of the drop is

known, we compute the volume averaged velocity of the drop as

$$U_i = \frac{1}{V} \int_V u_i dV = \frac{1}{V} \int_S (u_j n_j) x_i dS, \quad (63)$$

where  $V$  represents the volume of the drop, while  $\mathbf{n}$  is the unit normal vector at the surface. We computed the instantaneous volume averaged velocity of a spherical drop placed at  $y_c/H = 0.4$  and with a confinement ratio of  $2a/H = 0.6$  for different drop viscosity ratios  $\lambda$ . The simulation parameters for this calculation were kept the same as in the previous section, namely  $N_y = 61$ ,  $N_\Delta = 5120$ ,  $\alpha\Delta y_m = 0.44$ , and  $\Delta x_m = \Delta y_m = \Delta z_m$ . Just like in the case of rigid particle above, we again find the same  $L^{-2}$  scaling of the periodic image effects on the drop velocity. This is shown in Fig. (8a) for drops of different viscosity ratios  $\lambda$ , where the velocity of the drop has been non-dimensionalized by the corresponding velocity estimated for an infinite slit using the procedure outlined above in Sec. (6.1). Interestingly, for a drop with  $\lambda = 1$ , there is no observable periodicity effect, while the drop velocity increases with increasing  $L$  for  $\lambda > 1$  and decreases with increasing  $L$  for  $\lambda < 1$ . In Fig. (8b), we compare the results in the present work corrected for periodicity effects with those of Janssen and Anderson [28] for several different viscosity ratios ( $\lambda \in [0.5, 1, 2, 5]$ ). A very good agreement between our results and those reported by Janssen and Anderson [28] is evident at all viscosity ratios (error  $< 0.15\%$ ), thereby validating our implementation of the single and the double layer integral.

### 6.3. Validation of the capsule membrane mechanics and the overall implementation

We next consider a capsule in a simple shear flow. To enable comparison with literature results in an unbounded domain, we consider a large simulation box with  $L_x = H = L_z = 15a$ , where  $a$  is the radius of the initially spherical capsule placed at the center of the box. Other simulation parameters were:  $N_y = 97$ ,  $r_{cut} = 1.0$ ,  $\alpha\Delta y_m = 0.625$ ,  $N_\Delta = 5120$ , and  $\Delta x_m = \Delta y_m = \Delta z_m$ ; a convergence study with these parameters will be presented later in this section. The system is subjected to simple shear flow and we follow the evolution of the shape of capsule at various capillary numbers ( $Ca = \mu\dot{\gamma}a/G$ ) and viscosity ratios ( $\lambda$ ). Lac et al. [35] showed that a membrane lacking bending resistance buckles at high or low  $Ca$ ; the origin of this buckling has been shown to be numerical [39]. We saw a similar behavior and therefore restrict the results reported here to  $0.3 \leq Ca \leq 0.6$ . In this regime, the capsule shape evolution appeared to be stable with no apparent buckling. To characterize the shape of the deformed capsule, we introduce the commonly employed Taylor deformation parameter  $D$  defined as

$$D = \frac{L - B}{L + B}, \quad (64)$$

where  $L$  and  $B$  are the maximum and the minimum distance in the shear plane of a point on the surface of the capsule from its center. We use this as the definition of  $D$ , though some authors, e.g. Ramanujan and Pozrikidis [54], instead find a triaxial ellipsoid with the same inertia tensor as the given capsule, and then take  $L$  and  $B$  as the major and minor axis of that ellipsoid.

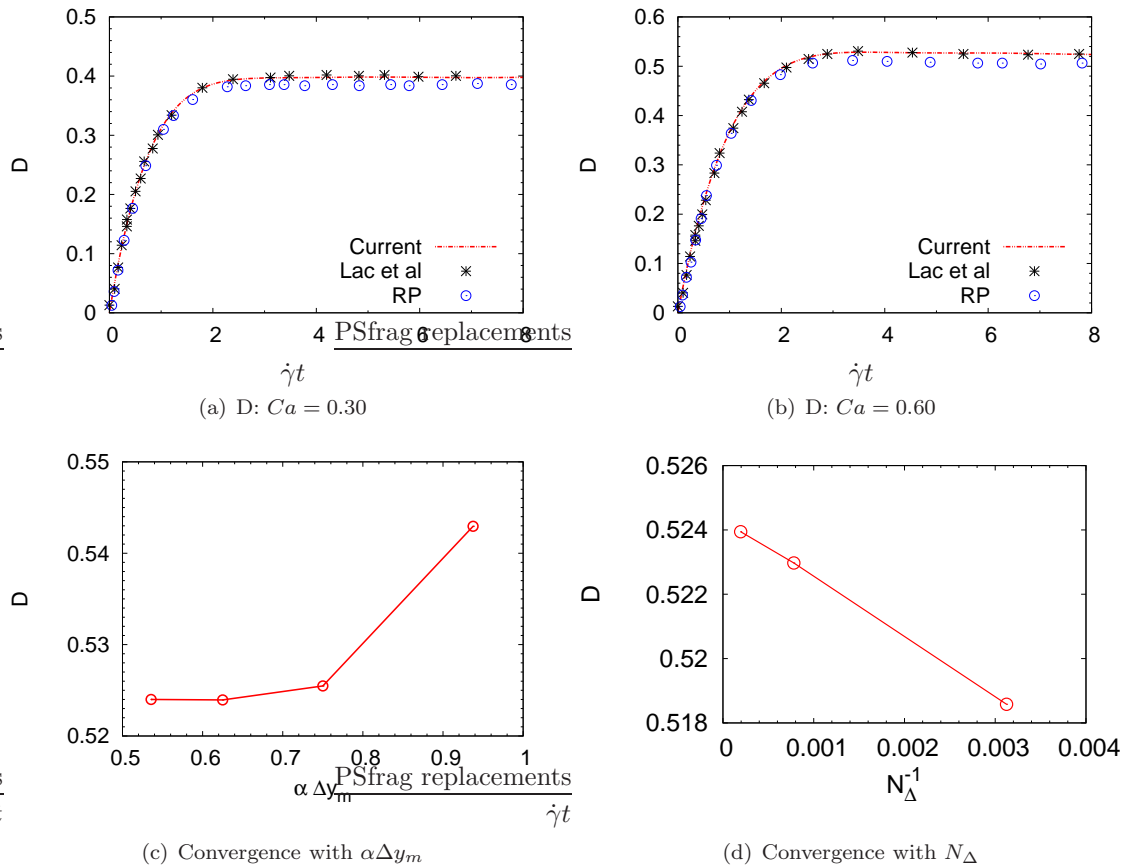


Figure 9:  $\lambda = 1$ : Time evolution of the Taylor deformation parameter  $D$  at (a)  $Ca = 0.3$  and (b)  $Ca = 0.6$ . Lac et al in the plot refers to the results of Lac et al. [35], while RP refers to the results of Ramanujan and Pozrikidis [54]. Simulation parameters were:  $L_x = L_y = H = 15a$ ,  $N_y = 97$ ,  $r_{cut} = a$ ,  $\alpha\Delta y_m = 0.625$ ,  $N_\Delta = 5120$ , and  $\Delta x_m = \Delta y_m = \Delta z_m$ . (c) Convergence of  $D$  at  $Ca = 0.6$  with respect to  $\alpha\Delta y_m$ . In this study  $r_{cut} = a$  was held fixed, while  $N_y$  was varied. (d) Convergence of  $D$  at  $Ca = 0.6$  with respect to  $N_\Delta$ . Rest of the parameters are the same as in (a) and (b).

The evolution of the deformation parameter  $D$  for a capsule with unit viscosity ratio ( $\lambda = 1$ ) is shown in Figs. (9a) and (9b) at two different capillary numbers  $Ca$ . The time in the figures has been non-dimensionalized by the shear rate. For comparison,  $D$  values reported by Ramanujan and Pozrikidis [54] and Lac et al. [35] are also plotted. Note that Ramanujan and Pozrikidis [54] have used a zero-thickness shell model for their capsules, though that gives only marginally lower deformation than a neo-Hookean capsule at the same  $Ca$  [54]. Moreover, they used the Young's modulus for computing their  $Ca$ , such that our results should be compared with their results at a  $Ca$  which is  $(1/3)$  of the  $Ca$  in this work. The data in Figs. (9a) and (9b) both show that the evolution of  $D$  in this work is in very good agreement with the corresponding results of Lac et al. [35]. Our results are also close to the values reported by Ramanujan and Pozrikidis [54], though the latter consistently display a slightly lower  $D$ . The broad agreement of  $D$  between our values and the literature values validates our implementation of the membrane mechanics along with other aspects of our method such as time-stepping and the already validated single layer integral.

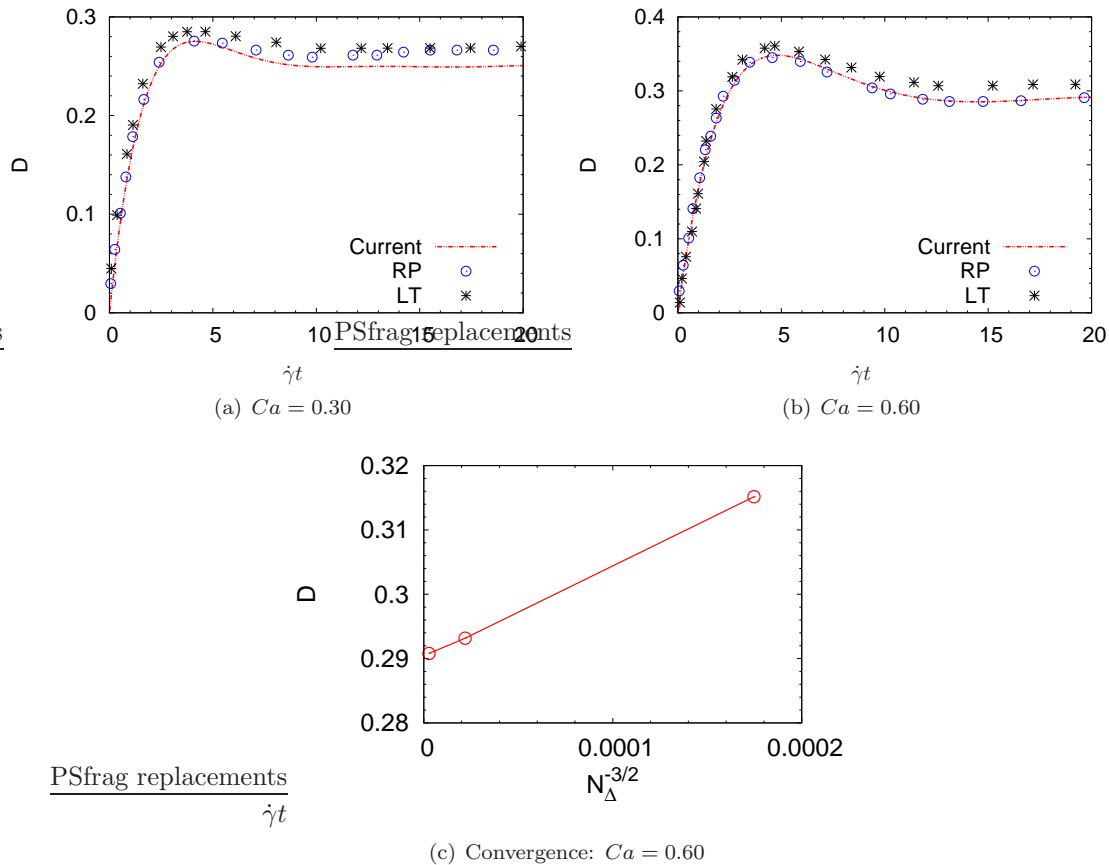


Figure 10:  $\lambda = 5$ : Time evolution of the Taylor deformation parameter  $D$  at (a)  $Ca = 0.3$  and (b)  $Ca = 0.6$ . Results from the present study are compared with the work of Ramanujan and Pozrikidis [54] (RP) and Le and Tan [38] (LT). Simulation parameters were the same as in Fig. (9). (c) Convergence of  $D$  with  $N_{\Delta}$  at  $Ca = 0.6$ .

Next, we demonstrate the convergence of the steady state  $D$  at  $Ca = 0.6$  with respect to the GGEM parameter  $\alpha\Delta y_m$  in Fig. (9c). For this calculation,  $r_{cut} = a$  was held fixed, while  $N_y$  was varied between 65 and 113. As could be seen, a convergence in  $D$  is observed at  $N_y = 97$  corresponding to  $\alpha\Delta y_m = 0.625$  – the parameter set for which all results are presented in this section. The convergence of the steady state  $D$  with respect to the number of triangular elements  $N_{\Delta}$  is demonstrated in Fig. (9d) for a  $Ca = 0.6$  capsule. The three data points in this plot correspond to simulations with  $N_{\Delta} = 320, 1280$  and  $5120$  elements. It is clear from this plot that the solution converges linearly with  $N_{\Delta}^{-1}$ , which is expected for linear elements.

We now briefly discuss the deformation parameter results for capsules with non-unit viscosity ratios (i.e.  $\lambda \neq 1$ ). These are reported in Fig. (10) for  $\lambda = 5$  and in Fig. (11) for  $\lambda = 0.2$ , and are compared with the results of Ramanujan and Pozrikidis [54] and Le and Tan [38], with the latter reference employing the immersed boundary technique for their simulations. At  $\lambda = 5$ , the results for  $D$  in the present work are slightly smaller than those reported by the previous authors at  $Ca = 0.3$ . At  $Ca = 0.6$ , an excellent agreement with the results of Ramanujan and Pozrikidis [54] is observed, though our results for  $D$  are slightly

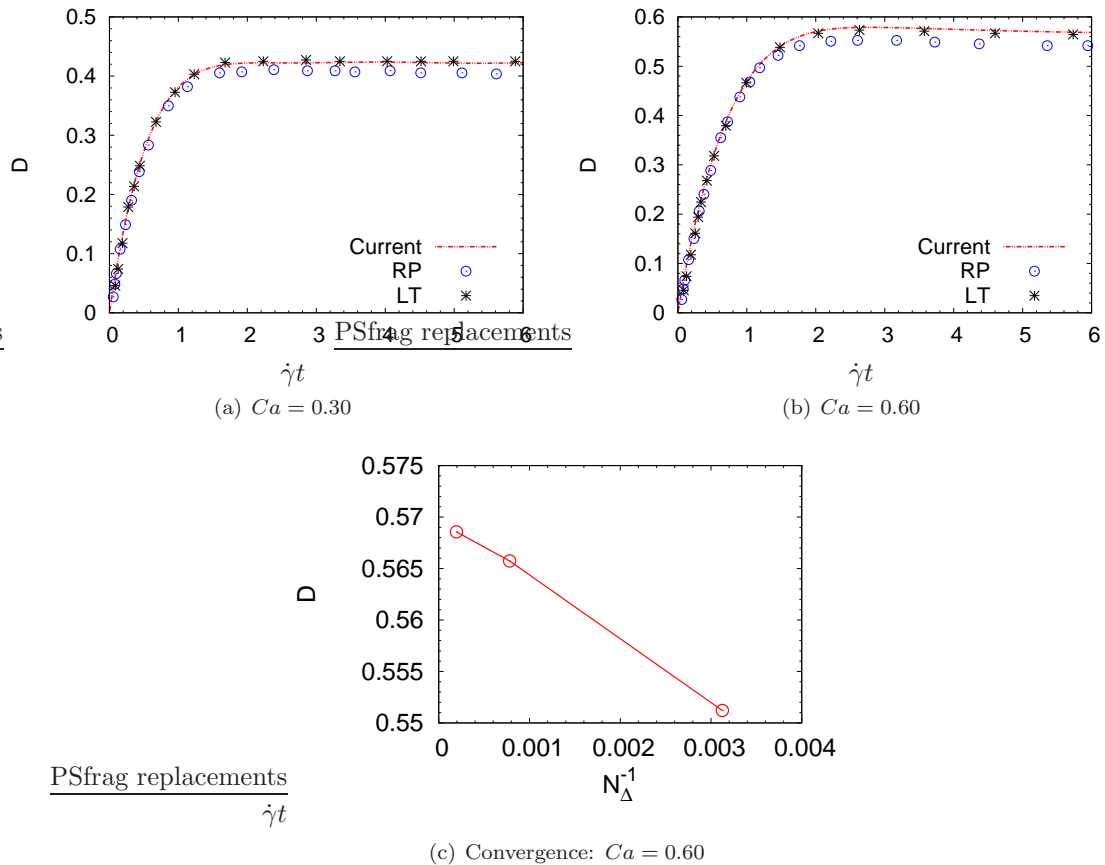


Figure 11:  $\lambda = 0.2$ : Time evolution of the Taylor deformation parameter at  $Ca = 0.3$  and (b)  $Ca = 0.6$ . Results from the current study are compared with the work of Ramanujan and Pozrikidis [54] (RP) and Le and Tan [38] (LT). Simulation parameters were the same as in Fig. (9). (c) Convergence of  $D$  at  $Ca = 0.6$  with  $N_{\Delta}$ .

lower than those of Le and Tan [38]. We next show the convergence of the steady state  $D$  at  $Ca = 0.6$  with respect to  $N_{\Delta}$  in Fig. (10c). These results indicate that the error decays as  $N_{\Delta}^{-3/2}$ , thereby implying that the error incurred in the calculation of the singular double layer integral dominates the overall error; see Sec. (3.5.2) for details.

We next discuss the results for the deformation parameter for capsules with  $\lambda = 0.2$  (Figs. 11a and 11b). In this case, we observe a very good agreement with the results of Le and Tan [38] at both  $Ca = 0.3$  and  $Ca = 0.6$ . The values reported by Ramanujan and Pozrikidis [54] are also close, though they are marginally lower than the results in the present study. Lastly, we show the convergence of the steady state  $D$  at  $Ca = 0.6$  with respect to  $N_{\Delta}$  in Fig. (11c). In this case the error is observed to decay at the expected rate of  $N_{\Delta}^{-1}$  – this probably implies that the error incurred in the calculation of the singular double layer integral is dominant only at high values of  $\lambda$ .

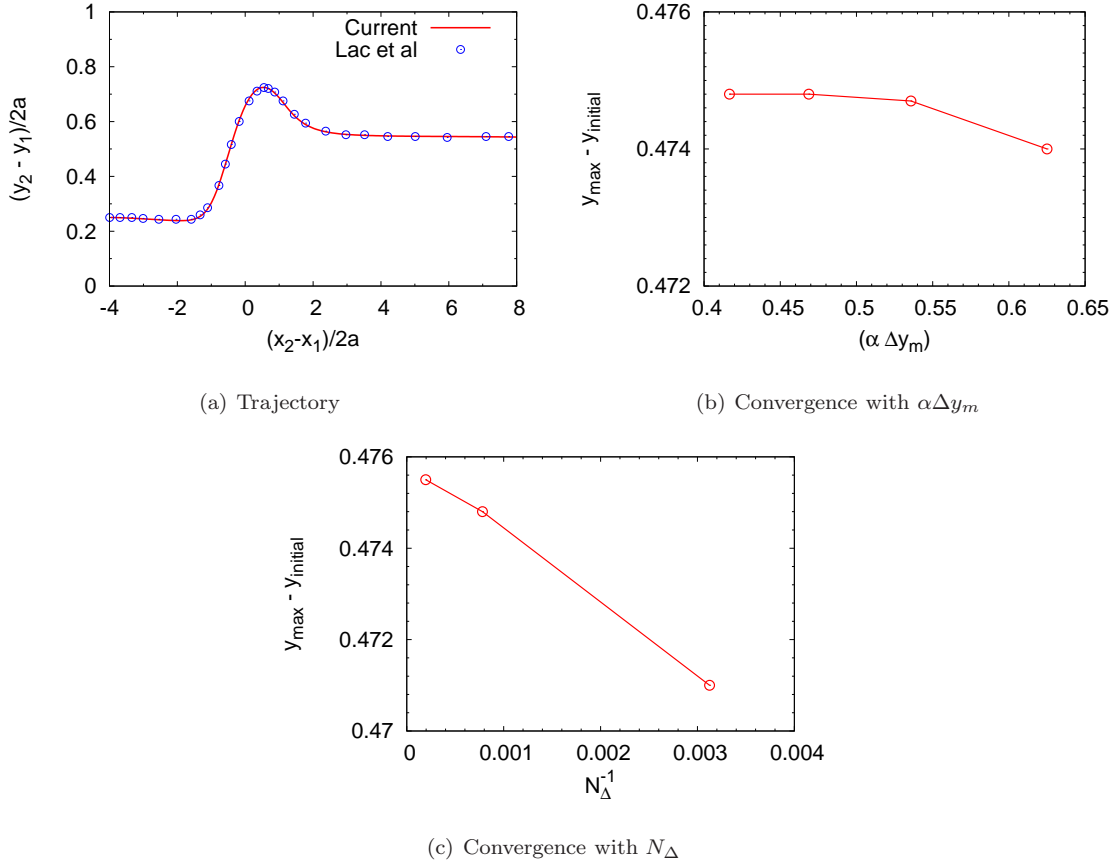


Figure 12: Pair collision:  $\lambda = 1$ . (a) Shows the separation between the centers of mass of capsules in the gradient direction as a function of their separation in the flow direction. Also plotted is the corresponding result from Lac et al. [36]. Simulation parameters were:  $L_x = L_y = H = 30a$ ,  $N_y = 129$ ,  $r_{cut} = 2a$ ,  $\alpha\Delta y_m = 0.469$ ,  $N_\Delta = 1280$ , and  $\Delta x_m = \Delta y_m = \Delta z_m$ . (b) Convergence of the maximum displacement of either particle (absolute value) from its initial position along the gradient direction ( $y$ ) as a function of  $\alpha\Delta y_m$ . Data points in this curve were obtained by holding  $r_{cut} = 2a$  fixed and varying  $N_y$ . (c) Convergence of the maximum absolute displacement of a particle in the gradient direction with  $N_\Delta$ .

#### 6.4. Pair collision

As a final test problem, we consider the collision between a pair of capsules with  $\lambda = 1$  in a simple shear flow and compare the results with the work of Lac et al. [36] in Fig. (12a). We first describe the problem setup. The size of the cubic box (slit) for this problem was set to  $30a$  to approximate an unbounded domain; simulations were performed with  $N_y = 129$ ,  $r_{cut} = 2a$ ,  $\alpha\Delta y_m = 0.469$ ,  $N_\Delta = 1280$ , and  $\Delta x_m = \Delta y_m = \Delta z_m$ . The two capsules were initially kept in the same flow-gradient plane ( $x - y$ ), such that the initial separation in the flow direction was  $x_2 - x_1 = -8a$ , while the initial offset in the gradient direction was  $y_2 - y_1 = 0.5a$ . As in Lac et al. [36], we preinflate the capsule by 5%, i.e. the radius of the spherical capsule was increased by 5% over its rest value, and this new increased radius is denoted by  $a$ . For a spherical shape, this inflation does not lead to any flow due to the incompressibility condition as discussed above in the case of a spherical drop. Nonetheless, this inflation keeps the membrane in a state of tension at rest and, if sufficient, will

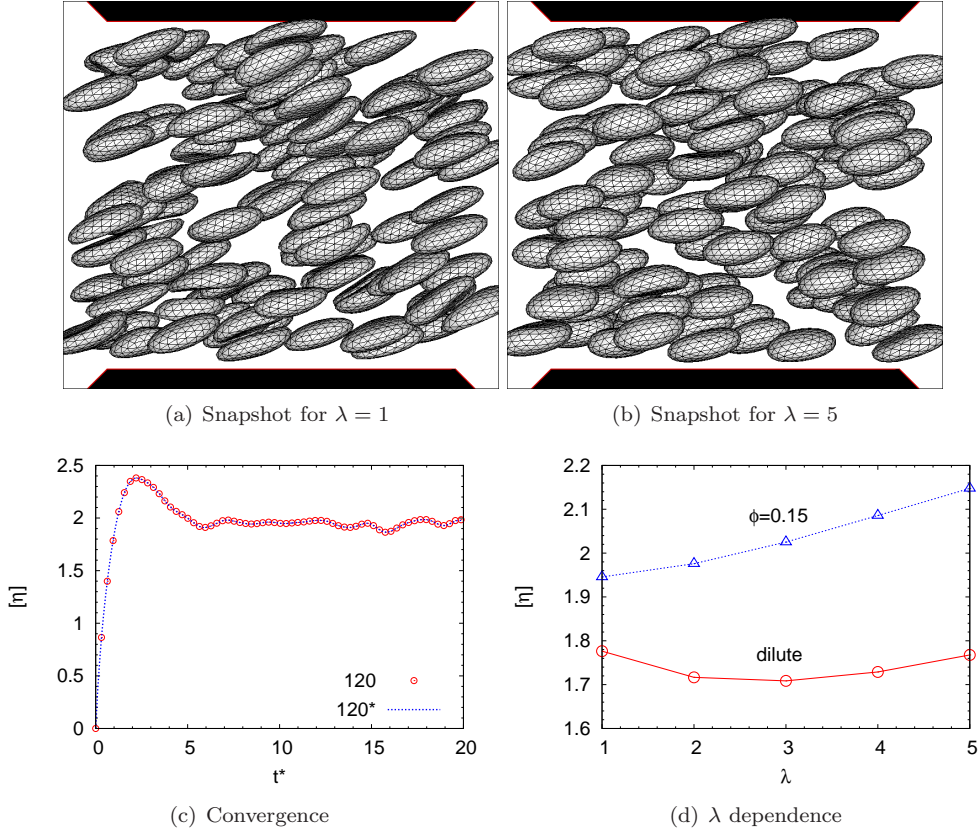


Figure 13: Suspensions of capsules at  $Ca = 0.5$  and volume fraction  $\phi = 0.15$ : (a) Snapshot of  $\lambda = 1$  capsule suspension with  $N_p = 120$ , (b) Snapshot of  $\lambda = 5$  capsule suspension with  $N_p = 120$ , (c) Convergence of the apparent intrinsic viscosity for  $\lambda = 1$  capsules in  $N_p = 120$  particle system. The simulation parameter  $\alpha\Delta y_m$  was 0.5 for the run labeled 120, while it was 0.417 for the run labeled 120\*, (d) Effect of  $\lambda$  on the apparent intrinsic viscosity for  $N_p = 120$  particle system. The simulation parameters in all cases above were:  $r_{cut} = a$ ,  $\alpha\Delta y_m = 0.5$ ,  $N_\Delta = 320$ , and  $\Delta x_m = \Delta y_m = \Delta z_m$  unless otherwise mentioned.

prevent buckling during the course of the collision. With these preliminaries, we return to Fig. (12a) where we show the relative separation between the center of masses in the gradient direction as a function of the corresponding separation in the flow direction. A very good agreement with the results of Lac et al. [36] is evident. Next, we show the convergence of the numerical scheme with  $\alpha\Delta y_m$  in Fig. (12b), where we plot the absolute value of the maximum displacement in the gradient direction for either particle. For this calculation  $r_{cut} = 2a$  was held fixed, while  $N_y$  was varied between 97 and 145. A convergence is seen at  $\alpha\Delta y_m = 0.469$  corresponding to  $N_y = 129$  – the parameters for which results are reported in this section. The convergence of the maximum displacement in the gradient direction with respect to  $N_\Delta$  is demonstrated in Fig. (12c), which confirms the expected error decay rate of  $N_\Delta^{-1}$ .

## 7. Multiparticle Simulations: suspension apparent viscosity and computational complexity

In this section, we report results from several large scale simulations on multiparticle suspensions of capsules. In the first part of the section, we present results for the suspension viscosity and discuss its

dependence on the viscosity ratio. In the second part, we discuss the expected computational complexity of the algorithm and verify it with timing results from the multiparticle simulations.

### 7.1. Suspension viscosity

We consider here a suspension of Neo-Hookean capsules in a cubic slit (Fig. 13a,b). These suspensions are subjected to a simple shear flow at a capillary number of  $Ca = 0.5$ ; the volume fraction of the suspension is  $\phi = 0.15$ , which is typical of the blood flow in the microcirculation [17]. Capsules with five different viscosity ratios  $\lambda$  are considered:  $\lambda = 1, 2, 3, 4$ , and  $5$ . The surface of each of the capsules was discretized into  $N_\Delta = 320$  triangular elements, while four different system sizes were considered with the number of particles being  $N_p = 15, N_p = 30, N_p = 60$ , and  $N_p = 120$ . In each of the problems,  $r_{cut} = a$  was kept fixed, where  $a$  is radius of the spherical capsule at rest. Similar to Sec. (6.4), the capsules were preinflated by 5% to prevent membrane buckling; the radius after preinflation is denoted by  $a$ . The number of mesh points  $N_y$  for the global solution varied between 61 and 121 such that  $\alpha\Delta y_m = 0.5$  in all cases with  $\Delta x_m = \Delta z_m = \Delta y_m$ . For testing the convergence of the results with respect to GGEM parameters, some simulations were also run with 20% extra mesh points in each of the directions corresponding to  $\alpha\Delta y_m = 0.417$ . We discuss next an important issue in multiparticle simulations, which concerns the treatment of near singular integrals – these integrals arise when the gaps between the particles become small.

In a suspension of particles subjected to shear, it is not uncommon to find particle pairs separated by a small gap. This is true, at least occasionally, even in suspensions with a moderate volume fraction such as  $\phi = 0.15$  studied here. When the gap between a particle pair becomes small, the interparticle contributions between such a pair from both the single as well as the double layer integrals become nearly singular; these nearly singular integrals require special treatment or the simulations may diverge [65]. In the literature, several techniques have been proposed to address this numerically difficult problem. A few among these are the near singularity subtraction technique [43, 65] and coordinate mapping techniques [47] for the evaluation of the near singular integrals. These techniques will, however, require very high surface mesh resolution and very high order quadrature techniques for the accurate evaluation of the nearly singular integrals [16, 62] – the cost associated with these requirements can be prohibitive. An alternative approach is the use of a short range repulsive force, which can prevent the formation of small gaps [16], though this is not very effective in three dimensional simulations [63]. The best approach appears to be an overlap correction in an auxiliary step [63]. This approach is also frequently used in suspensions of rigid particles [15, 45, 32]. In the present work, like in past efforts [45, 63], we not only correct the overlaps, but also maintain a minimum gap ( $h_s^m$ ) between the surfaces of two particles. This approach was also employed in our recent work [31]. For simulations in the current section, we set the minimum gap parameter to a small value of  $h_s^m = 0.05a$ .

The overlap correction procedure employed in this work involves moving a pair of overlapping particles apart along their line of centers like a rigid particle until the minimum gap requirement is satisfied. Trans-

lating the capsules like a rigid particle in this auxiliary step has the benefit that the shapes of the particles remain unchanged, as is the orientation of the particles with respect to the flow. In general, multiple steps of the correction procedure is required, as the correction of overlap between one pair could result in other overlaps [15, 45]. This overlap correction step involves minimal displacement of the particles, on the order of  $h_s^m$ . Given that the volume fraction studied in this work is  $\phi = 0.15$ , this procedure was rarely required – on an average, less than 0.1 particle pairs in the  $N_p = 120$  particle system exhibited minimum gap violations at any given time. We finally remark that apart from correcting the minimum gap violations in the system, no special treatment was accorded to the evaluation of the near singular integrals in the present effort.

Having discussed the procedure for controlling the minimum gap in the system, we now turn to the results from multiparticle simulations. All these simulations were initiated by placing the particles randomly in the simulation box, and then they were sheared for a total non-dimensional time of  $t^* = \dot{\gamma}t = 20$ . We show some representative snapshots from 120 particle simulations in Figs. (13a) and (13b) for  $\lambda = 1$  and  $\lambda = 5$  capsules, respectively. It is immediately obvious from these snapshots that the more viscous capsules deform less and also have a smaller inclination angle with the flow direction; both of these observations are similar to observations in isolated sheared capsules [54]. The convergence of the simulation with respect to GGEM parameters is demonstrated in Fig. (13c), where we plot the suspension apparent intrinsic viscosity  $[\eta]$  for  $\lambda = 1$  capsule and  $N_p = 120$  particle system for two different mesh resolutions corresponding to  $\alpha\Delta y_m = 0.5$  and  $\alpha\Delta y_m = 0.417$ . The apparent intrinsic viscosity is defined as  $[\eta] = \Sigma_{xy}^p / (\mu\dot{\gamma}\phi)$ , where  $\Sigma_{xy}^p$  is the particle contribution to shear stress, while  $\mu$  is the suspending fluid viscosity. The particle contribution to the stress tensor is given by [29]

$$\Sigma_{ij}^p = \frac{1}{V} \sum_{m=1}^{N_p} \int_{S_m} [\Delta f_i x_j + \mu(\lambda - 1)(u_i n_j + u_j n_i)] dS, \quad (65)$$

where the sum in the right hand side is over all the particles in the system. As can be seen in Fig. (13c),  $[\eta]$  is nearly identical for simulations run with  $\alpha\Delta y_m = 0.5$  and  $\alpha\Delta y_m = 0.417$ , thereby demonstrating the convergence of the simulation with respect to GGEM parameters. All the remaining simulations were performed with  $\alpha\Delta y_m = 0.5$ . The effect of viscosity ratio on the apparent intrinsic viscosity is shown in Fig. (13d). These results represent an average over the last 10 time units in the  $N_p = 120$  particle systems, which have a confinement ratio of  $2a/H = 0.134$ . For a direct comparison, the plot also shows  $[\eta]$  for a dilute suspension of capsules obtained from single particle simulations in the same geometry. In dilute suspensions, a non-monotonic variation of the viscosity with  $\lambda$  is obvious – this behavior has been demonstrated before in the literature [2]. However, the non-monotonicity vanishes at the non-dilute volume fraction of  $\phi = 0.15$ . This indicates that the contribution to the overall stress from particle-particle interactions is a monotonically increasing function of  $\lambda$ , and, in non-dilute suspensions, easily compensates the non-monotonic variation of the isolated particle contribution. Hence caution is warranted before extrapolating trends from dilute systems to non-dilute systems like blood flow.

## 7.2. Computational complexity

We devote the remainder of this section to analyzing the overall computational complexity of our algorithm. Before presenting the timing results from the detailed numerical simulations presented above, it will be useful to first discuss the expected computational cost associated with various steps in the algorithm, and consequently the overall implementation. The first step in the solution procedure, as discussed in Sec. (5), involves iteratively solving for the single layer density  $\mathbf{q}^b$  (step 1). This is followed by the computation of the fluid velocity  $\mathbf{u}^b$  at the element nodes (step 2) using the single layer density  $\mathbf{q}^b$  computed in the previous step. The computational cost associated with each iteration of step 1 and that of step 2 has an identical optimal scaling with  $N = N_\Delta \times N_p$ , each of which is essentially determined by the computational cost associated with the Stokes flow solver (GGEM) described in Sec (3.2). Therefore, for a direct cost comparison with the multiparticle flow problem here, we consider an auxiliary problem involving a collection of  $N$  point forces; both problems then have an identical computational cost scaling with  $N$ . At this stage, it will also be worth pointing out that the computational complexity analysis presented here closely follows the corresponding analysis in PME like methods [40, 41] as the underlying ideas are fairly similar.

The overall cost associated with the GGEM Stokes flow solver is the sum of costs associated with the local problem and the global problem. The cost of the local solution scales as the product of the number of point forces  $N$  and the number of neighbors within a distance  $r_{cut} \sim \alpha^{-1}$  of each of the point forces. If we require the computational cost of the local problem to scale as  $t_l \sim O(N)$ , then the number of neighbors per point force must stay constant with changing system size (meaning  $N$  here). The system size  $N$  can be increased in two contrasting ways: (i) by increasing volume at constant density (i.e., by increasing  $V$  while maintaining  $N/V$  constant,  $V$  is the system volume), and (ii) by increasing density at constant volume (i.e., by increasing  $N/V$  while maintaining  $V$  constant). If the system size is increased at constant density, we require that  $\alpha$  (or  $r_{cut}$ ) be held constant, and if the system size is increased at constant volume, we require that  $\alpha \sim N^{1/3}$  (or  $r_{cut} \sim N^{-1/3}$ ). This scheme for choosing  $\alpha$  ensures that the average number of near neighbors per point force is independent of the system size. Hence, irrespective of how  $N$  is varied, we always obtain  $t_l \sim O(N)$ . Next, we determine the computational cost of the global solution procedure. Before we proceed further, it is important to realize that the error in the global solution is essentially controlled by the parameter  $\alpha \Delta y_m$ <sup>1</sup>; see Sec. (3.2.2). Therefore, for the error in the global solution to remain of the same order with changing system size  $N$ , we require that  $\alpha \Delta y_m$  be held constant; this implies  $\Delta y_m \sim \alpha^{-1}$ . Coupling this requirement with the choices of  $\alpha$  discussed above in different scenarios, we conclude that the total number of mesh points involved in the calculation of the global solution  $n = N_x N_y N_z$  must be varied proportionally to  $N$ , i.e.  $n \sim N$ . Having determined the scaling of  $n$ , we next present the expression for the

---

<sup>1</sup>the error in the local solution is set by the choice of the parameter  $\alpha r_{cut}$ , which is unchanged with changing  $N$

computational cost of the global solution  $t_g$  as follows:

$$t_g \sim \frac{n}{N_x} O(N_x \log N_x) + \frac{n}{N_z} O(N_z \log N_z) + \frac{n}{N_y} (O(N_y) + O(N_y \log N_y)), \quad (66)$$

where the first two terms on the right hand side denote the cost associated with the FFT operations in  $x$  and  $z$  directions respectively, while the last term is associated with the cost of the Chebyshev-tau solver in the wall normal  $y$  direction. Note that the  $O(N_y)$  cost in the expression for the Chebyshev-tau solver is associated with the quasi-tridiagonal solve, while  $O(N_y \log N_y)$  cost is associated with the computation of the Chebyshev transforms and its inverse with FFTs. Simplifying the above expression and noting that  $n \sim N$ , we obtain the following asymptotic scaling

$$t_g \sim n \log n \sim N \log N. \quad (67)$$

The overall cost per iteration of step 1 or of step 2 is therefore,

$$t = t_l + t_g \sim O(N) + O(N \log N) \sim N \log N. \quad (68)$$

The total cost of step 1 is the cost per iteration times the number of iterations required for convergence. Now, if the number of iterations in step 1 is independent of  $N$ , then the computational cost of the overall algorithm will scale as  $N \log N$ . On the other hand, if the number of iterations in step 1 is dependent on the system size, say it scales as  $N^e$ , then the computational cost of the overall algorithm will scale as:

$$t \sim N^{1+e} \log N. \quad (69)$$

Note that the need for iterative solution of step 1 or a related second kind integral equation is not unique to the present formulation, but is a general feature of any accelerated boundary integral method with  $\lambda \neq 1$  [63].

Having determined the expected scaling of our algorithm, we next report timing results from the detailed numerical simulations presented in Sec. (7.1). All runs were performed on a single core of a eight core machine with a 2 GHz Intel Xeon processor running Linux. We plot the time required per stage of the two stage midpoint time stepping algorithm in Fig. (14). Note that the abscissa in the plot is  $N_p \log N_p$ ; the four data points in this plot are respectively for  $N_p = 15$ ,  $N_p = 30$ ,  $N_p = 60$  and  $N_p = 120$  as discussed above. One can conclude from this plot that in all cases the computational cost scales approximately as  $t \sim N_p \log N_p$  (in fact, in this case, the increase in the computational cost appears to be slower than the expected  $N_p \log N_p$ ). Another important feature to note in the plot is the jump in computational cost as one moves from a matched viscosity problem to a non-matched one, which is expected as no iterations are required in matched viscosity problems. The number of iterations required for convergence was found to be independent of the system size for problems considered here, though it was found to increase with

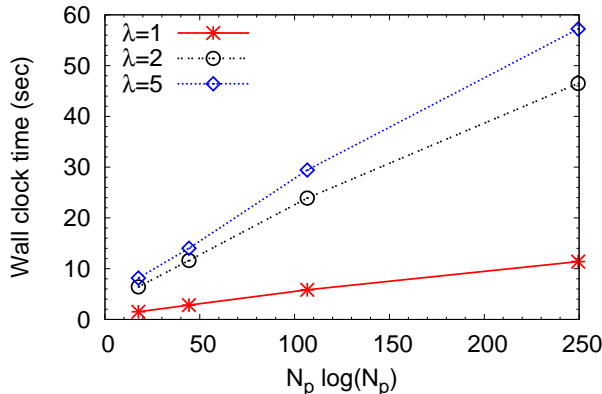


Figure 14: Wall clock time per stage of a two stage midpoint method for various viscosity ratios  $\lambda$  and for various system sizes. The four data points in the plot correspond to  $N_p = 15, 30, 60,$  and  $120$  respectively. Note that the time is plotted against  $N_p \log N_p$ .

increasing  $\lambda$ . The simulations with  $\lambda = 2$  capsules required approximately 2 iterations on an average, while the simulations with  $\lambda = 5$  capsules required approximately 3 iterations. To summarize this section, we note that a near perfect scaling of  $N \log N$  is obtained for both matched viscosity and non-matched viscosity problems. A few words of caution are necessary here, though, as at higher volume fractions and/or at much larger system sizes, the number of iterations for convergence is expected to become system size dependent. It must be emphasized here that this aspect is not specific to our implementation, but is intrinsic to the boundary integral equation for non-matched viscosity problems. Future work on enhancements in the algorithm should address this by the development of efficient preconditioners. Another obvious enhancement in the algorithm will be its parallelization to take advantage of cheaply available multicore processors.

## 8. Conclusions

A new accelerated boundary integral method for multiphase Stokes flow in a confined geometry was presented. The complexity of the method scales as  $O(N \log N)$  for the slit geometry discussed in the present paper. The acceleration in the method was provided by the use of General Geometry Ewald-like (GGEM) method for the fast computation of the velocity and stress fields driven by a set of point forces in the geometry of interest. Due to non-periodic nature of the domain, an alternative boundary integral formulation was employed, necessitated by the requirements of the acceleration technique. An efficient methodology was presented to compute the resulting double and single layer integrals using the GGEM technique. The resulting implementation was validated with several test problems. The computational complexity of the algorithm was verified to be  $O(N \log N)$  with timing results from several large scale multiparticle simulations.

## **Acknowledgments**

The authors gratefully acknowledge helpful discussions with Pratik Pranay, Yu Zhang and Juan Hernandez-Ortiz on the implementation of GGEM. This work was supported by NSF Grants CBET-0852976 and CBET-1132579.

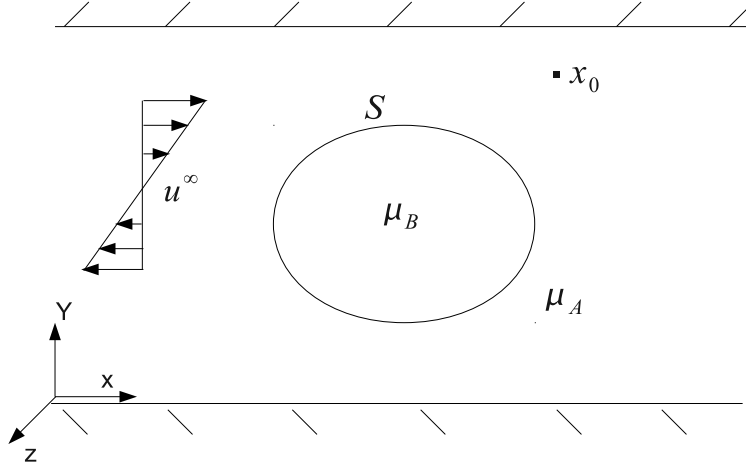


Figure 15: Schematic of the problem described in Appendix A. The figure shows the dispersed phase with viscosity  $\mu_A$  and a particle with viscosity  $\mu_B$ . The surface of the particle is denoted by  $S$ . Also shown is the undisturbed flow denoted by  $\mathbf{u}^\infty$ .

## Appendix A. Derivation of Boundary Integral equation

Consider a two phase flow in a specified geometry as shown in Fig. (1). The two fluids are respectively denoted by  $A$  and  $B$  in the figure with viscosity  $\mu_A$  and  $\mu_B$ . The fluid  $B$  is assumed to be enclosed by an impermeable interface denoted by  $S$ , which has its own characteristic properties (e.g. drops, capsules, vesicles, etc). Now, consider a point  $\mathbf{x}_0$  in fluid  $A$  as shown in Fig. (15). Applying the reciprocal theorem to the disturbance velocity in the region  $A$  denoted by  $\mathbf{u}^{DA} = \mathbf{u}^A - \mathbf{u}^\infty$ , and that due to a point force located at  $\mathbf{x}_0$ , we obtain

$$u_j^{DA}(\mathbf{x}_0) = \frac{-1}{8\pi\mu_A} \int_S f_i^{DA}(\mathbf{x}) G_{ij}(\mathbf{x}, \mathbf{x}_0) dS(\mathbf{x}) + \frac{1}{8\pi} \int_S u_i^{DA}(\mathbf{x}) T_{ijk}(\mathbf{x}, \mathbf{x}_0) n_k(\mathbf{x}) dS(\mathbf{x}), \quad (\text{A.1})$$

where  $\mathbf{f}^{DA}$  is the hydrodynamic traction at the interface on the side of fluid  $A$  associated with the velocity field  $\mathbf{u}^{DA}$ , while  $\mathbf{G}$  is the Green's function for the specified geometry and  $\mathbf{T}$  is the associated stress tensor. Next, employing the self-adjointness property of the Green's function  $\mathbf{G}$ , we obtain the following form of the above equation

$$u_j^{DA}(\mathbf{x}_0) = \frac{-1}{8\pi\mu_A} \int_S f_i^{DA}(\mathbf{x}) G_{ji}(\mathbf{x}_0, \mathbf{x}) dS(\mathbf{x}) + \frac{1}{8\pi} \int_S u_i^{DA}(\mathbf{x}) T_{ijk}(\mathbf{x}, \mathbf{x}_0) n_k(\mathbf{x}) dS(\mathbf{x}). \quad (\text{A.2})$$

Recall that the self-adjointness of the Green's function  $\mathbf{G}$  implies that

$$G_{ij}(\mathbf{x}, \mathbf{x}_0) = G_{ji}(\mathbf{x}_0, \mathbf{x}). \quad (\text{A.3})$$

Next, we apply the reciprocal theorem to the undisturbed flow  $\mathbf{u}^\infty$  in region  $B$  and due to a point force located at  $\mathbf{x}_0$  in region  $A$ . This yields,

$$0 = \int_S f_i^{B\infty}(\mathbf{x}) G_{ji}(\mathbf{x}_0, \mathbf{x}) dS(\mathbf{x}) - \mu_B \int_S u_i^\infty(\mathbf{x}) T_{ijk}(\mathbf{x}, \mathbf{x}_0) n_k(\mathbf{x}) dS(\mathbf{x}) \quad (\text{A.4})$$

Note that in the above equation, the normal  $\mathbf{n}$  is pointing out of region  $B$  into region  $A$  (outward normal). We next note the following relation between  $\mathbf{f}^{A\infty}$  and  $\mathbf{f}^{B\infty}$

$$\frac{\mathbf{f}^{B\infty}}{\mu_B} = \frac{\mathbf{f}^{\infty}}{\mu_A}. \quad (\text{A.5})$$

This follows from the continuity of the undisturbed flow across the interface, and that the internal and external stresses are computed with viscosity  $\mu_B$  and  $\mu_A$  respectively for the same flow field. Using this relationship, we write Eq. (A.4) as

$$0 = -\frac{1}{8\pi\mu_A} \int_S f_j^{A\infty}(\mathbf{x}) G_{ji}(\mathbf{x}_0, \mathbf{x}) dS(\mathbf{x}) + \frac{1}{8\pi} \int_S u_i^{\infty}(\mathbf{x}) T_{ijk}(\mathbf{x}, \mathbf{x}_0) n_k(\mathbf{x}) dS(\mathbf{x}). \quad (\text{A.6})$$

Adding Eqs. (A.2) and (A.6), we obtain

$$8\pi\mu_A u_j^{DA}(\mathbf{x}_0) = -\int_S f_i^A(\mathbf{x}) G_{ji}(\mathbf{x}_0, \mathbf{x}) dS(\mathbf{x}) + \mu_A \int_S u_i^A(\mathbf{x}) T_{ijk}(\mathbf{x}, \mathbf{x}_0) n_k(\mathbf{x}) dS(\mathbf{x}). \quad (\text{A.7})$$

Next, we apply reciprocal theorem to the fluid velocity in region 2 ( $\mathbf{u}^B$ ) and due to a point force located at  $\mathbf{x}_0$ . This yields

$$0 = \int_S f_j^B(\mathbf{x}) G_{ji}(\mathbf{x}_0, \mathbf{x}) dS(\mathbf{x}) - \mu_B \int_S u_i^B(\mathbf{x}) T_{ijk}(\mathbf{x}, \mathbf{x}_0) n_k(\mathbf{x}) dS(\mathbf{x}). \quad (\text{A.8})$$

For interfacial flows neither the interfacial velocity nor the interface tractions on either side is known, though we have the following boundary conditions at any point on the interface

$$\mathbf{u}^A = \mathbf{u}^B = \mathbf{u}^I \quad (\text{A.9a})$$

$$\Delta f = \mathbf{f}^A - \mathbf{f}^B = -\mathbf{f}^I, \quad (\text{A.9b})$$

which essentially implies the continuity of the velocity across the interface and that the net force on an element due to hydrodynamic stresses is balanced by the net force due to interfacial stresses, see Sec. (4). We note that the interfacial contribution  $\mathbf{f}^I$  is assumed to be known by the known constitutive equation of the interface and its known configuration. Given the unknowns and the boundary conditions, a very common approach is to eliminate the unknown hydrodynamic interfacial tractions  $\mathbf{f}^A$  and  $\mathbf{f}^B$  with the known traction jump  $\Delta f$  in Eqs. (A.7) and (A.8). This leads to the widely employed second kind integral equation for the unknown interfacial velocity. Here, we adopt an alternative approach. Using Eqs (A.7) and (A.8) we instead eliminate the double layer integral to obtain

$$8\pi\mu_j^{DA}(\mathbf{x}_0) = -\frac{1}{\mu_A} \int_S f_i^A(\mathbf{x}) G_{ji}(\mathbf{x}_0, \mathbf{x}) dS(\mathbf{x}) + \frac{1}{\mu_B} \int_S f_i^B(\mathbf{x}) G_{ji}(\mathbf{x}_0, \mathbf{x}) dS(\mathbf{x}). \quad (\text{A.10})$$

The above can be written in the following form

$$u_j(\mathbf{x}_0) = u_j^{\infty}(\mathbf{x}_0) + \frac{1}{8\pi} \int_S \left( \frac{f_i^B(\mathbf{x})}{\mu_B} - \frac{f_i^A(\mathbf{x})}{\mu_A} \right) G_{ji}(\mathbf{x}_0, \mathbf{x}) dS(\mathbf{x}). \quad (\text{A.11})$$

This equation for the velocity can be shown to be valid inside, outside, as well as on the boundary  $S$ . The drawback of this equation is that both the velocity (including interfacial velocity) and the surface tractions are unknown. The main advantage for our purposes here is that we have switched the pole and the field point of the Green's function using its self-adjointness property (Eq. A.3). For simplifying the notation, we next express the operand of the Green's function by  $\mathbf{q}$ , i.e. we define  $\mathbf{q}$  as

$$\mathbf{q}(\mathbf{x}) = \frac{1}{8\pi} \left( \frac{\mathbf{f}^B(\mathbf{x})}{\mu_2} - \frac{\mathbf{f}^A(\mathbf{x})}{\mu_1} \right). \quad (\text{A.12})$$

Using the above definition, we write the velocity as

$$u_j(\mathbf{x}_0) = u_j^\infty(\mathbf{x}_0) + \int_S q_i(\mathbf{x}) G_{ji}(\mathbf{x}_0, \mathbf{x}) dS(\mathbf{x}). \quad (\text{A.13})$$

The pressure associated with the above velocity field in the region external to  $S$  can be written as

$$p(\mathbf{x}_0) = p^\infty(\mathbf{x}_0) + \mu_A \int_S q_i(\mathbf{x}) P_i(\mathbf{x}_0, \mathbf{x}) dS(\mathbf{x}). \quad (\text{A.14})$$

Using Eqs. (A.13) and (A.14), we can write the stress  $\sigma_{jk}^A(\mathbf{x}_0)$  as

$$\sigma_{jk}^A(\mathbf{x}_0) = \sigma_{jk}^{A\infty}(\mathbf{x}_0) + \mu_A \int_S q_i(\mathbf{x}) T_{jik}(\mathbf{x}_0, \mathbf{x}) dS(\mathbf{x}) \quad (\text{A.15})$$

A similar expression can be written for  $\sigma_{jk}^B(\mathbf{x}_0)$  as shown below:

$$\sigma_{jk}^B(\mathbf{x}_0) = \sigma_{jk}^{B\infty}(\mathbf{x}_0) + \mu_B \int_S q_i(\mathbf{x}) T_{jik}(\mathbf{x}_0, \mathbf{x}) dS(\mathbf{x}) \quad (\text{A.16})$$

We will now take the limit of the above equations as we approach the interface from either side and then dot it with the normal to get the tractions on either side of the interface  $\mathbf{f}^A$  and  $\mathbf{f}^B$ . We can express both of them using the principal value of the double layer integral along with the jump condition to obtain [50]

$$f_j^A(\mathbf{x}_0) = f_j^{A\infty}(\mathbf{x}_0) - 4\pi\mu_A q_j(\mathbf{x}_0) + \mu_A n_k(\mathbf{x}_0) \int_S^{PV} q_i(\mathbf{x}) T_{jik}(\mathbf{x}_0, \mathbf{x}) dS(\mathbf{x}), \quad (\text{A.17a})$$

$$f_j^B(\mathbf{x}_0) = f_j^{B\infty}(\mathbf{x}_0) + 4\pi\mu_B q_j(\mathbf{x}_0) + \mu_B n_k(\mathbf{x}_0) \int_S^{PV} q_i(\mathbf{x}) T_{jik}(\mathbf{x}_0, \mathbf{x}) dS(\mathbf{x}), \quad (\text{A.17b})$$

where  $PV$  implies the principal value of the improper integral when the observation point lies on the domain of the integration. Note that the sign of the jump condition ( $4\pi q_j(\mathbf{x}_0)$ ) depends on the direction from which we approach the interface relative to the outward normal defined above, i.e. whether we approach the interface parallel to the normal or anti to it.

Taking the difference of Eqs. (A.17a) from (A.17b) and using Eqs. (A.9b) and (A.5), we have that

$$-\Delta f_j(\mathbf{x}_0) = (\lambda - 1) f_j^{A\infty}(\mathbf{x}_0) + 4\pi\mu_A (\lambda + 1) q_j(\mathbf{x}_0) + (\lambda - 1)\mu_A n_k(\mathbf{x}_0) \int_S^{PV} q_i(\mathbf{x}) T_{jik}(\mathbf{x}_0, \mathbf{x}) dS(\mathbf{x}), \quad (\text{A.18})$$

where we have now introduced the viscosity ratio  $\lambda = \mu_B/\mu_A$ . Rearranging the above equation, we obtain

a second kind integral equation for the density of the Green's function  $\mathbf{q}$  as follows:

$$q_j(\mathbf{x}_0) + \frac{\kappa}{4\pi} n_k(\mathbf{x}_0) \int_S^{PV} q_i(\mathbf{x}) T_{jik}(\mathbf{x}_0, \mathbf{x}) dS(\mathbf{x}) = -\frac{1}{4\pi\mu_A} \left( \frac{\Delta f_j(\mathbf{x}_0)}{\lambda + 1} + \kappa f_j^{A\infty}(\mathbf{x}_0) \right), \quad (\text{A.19})$$

where we have defined  $\kappa$  as

$$\kappa = \frac{\lambda - 1}{\lambda + 1}. \quad (\text{A.20})$$

The above equation is used to solve for the unknown density  $\mathbf{q}$ , which upon substitution in Eq. (A.13) gives the velocity at any point in the domain, including the interface.

## Appendix B. Undisturbed flow stress

For pressure driven flows, the stress tensor is given by

$$\sigma_{ij}^\infty = \frac{8\mu U_0}{H^2} x \delta_{ij} + \frac{4\mu U_0}{H} \left(1 - \frac{2y}{H}\right) e_{ij}, \quad (\text{B.1})$$

where  $e_{ij}$  is

$$\mathbf{e} = \begin{pmatrix} 0 & 1 & 0 \\ 1 & 0 & 0 \\ 0 & 0 & 0 \end{pmatrix}. \quad (\text{B.2})$$

Note that the velocity and pressure field in pressure driven flows is given by the following expressions

$$u = 4U_0 \frac{y}{H} \left(1 - \frac{y}{H}\right), \quad (\text{B.3a})$$

$$p = -\frac{8\mu U_0}{H^2} x. \quad (\text{B.3b})$$

In the above equations,  $U_0$  is the centerline velocity. The surface traction  $\mathbf{f}^\infty(\mathbf{x})$  can be obtained at a point  $\mathbf{x}$  on the surface with normal vector  $\mathbf{n}(\mathbf{x})$  as

$$f_i^\infty(\mathbf{x}) = \sigma_{ij}^\infty(\mathbf{x}) n_j(\mathbf{x}). \quad (\text{B.4})$$

For simple shear flows, the stress tensor is given by

$$\sigma_{ij}^\infty = \mu \dot{\gamma} e_{ij}, \quad (\text{B.5})$$

where  $\dot{\gamma}$  is the shear rate. The surface traction for this case can be obtained by substituting the stress tensor in the above equation in Eq. (B.4).

## Appendix C. Fast Spectral Stokes Flow Solver

Here we discuss the solution procedure for the global problem in Eq. (10) for a slit geometry (Fig. 1). We simplify the notation in Eq. (10) and represent it by the following set of equations:

$$-\nabla p(\mathbf{x}) + \mu \nabla^2 \mathbf{u}(\mathbf{x}) = \mathbf{f}(\mathbf{x}), \quad (\text{C.1a})$$

$$\nabla \cdot \mathbf{u}(\mathbf{x}) = 0, \quad (\text{C.1b})$$

where  $p$  is the pressure,  $\mathbf{u} = (u, v, w)$  is the velocity, while  $\mathbf{f}(\mathbf{x}) = (f_x, f_y, f_z)$  is a known function obtained from the known distribution of global force densities. The above set of equations are supplemented by the periodic boundary conditions in  $x$  and  $z$  directions, while a Dirichlet boundary condition for the velocity is specified in the  $y$  direction:

$$\mathbf{u}(x, z) = \mathbf{g}_1(x, z) \text{ at } y = 0, \quad (\text{C.2a})$$

$$\mathbf{u}(x, z) = \mathbf{g}_2(x, z) \text{ at } y = H. \quad (\text{C.2b})$$

The velocity and pressure variables are first expanded in truncated Fourier series in  $x$  and  $z$  directions as:

$$u(\mathbf{x}) = \sum_{l=-N_x/2}^{N_x/2-1} \sum_{m=-N_z/2}^{N_z/2-1} \hat{u}_{lm}(y) e^{i2\pi l x/L_x} e^{i2\pi m z/L_z}. \quad (\text{C.3})$$

Similar expressions are written for  $v(\mathbf{x})$ ,  $w(\mathbf{x})$ ,  $p(\mathbf{x})$ ,  $f_x(\mathbf{x})$ ,  $f_y(\mathbf{x})$ , and  $f_z(\mathbf{x})$  by replacing  $\hat{u}_{lm}$  by  $\hat{v}_{lm}$ ,  $\hat{w}_{lm}$ ,  $\hat{p}_{lm}$ ,  $\hat{f}_{xlm}$ ,  $\hat{f}_{ylm}$ , and  $\hat{f}_{zlm}$  respectively in the above equation. Substituting this in equation (C.1) and employing the Galerkin method, we obtain the following owing to the orthogonality of Fourier modes:

$$-il\hat{p} - \mu(k^2 - \frac{\partial^2}{\partial^2 y})\hat{u} = \hat{f}_x, \quad (\text{C.4a})$$

$$-\frac{\partial \hat{p}}{\partial y} - \mu(k^2 - \frac{\partial^2}{\partial^2 y})\hat{v} = \hat{f}_y, \quad (\text{C.4b})$$

$$-im\hat{p} - \mu(k^2 - \frac{\partial^2}{\partial^2 y})\hat{w} = \hat{f}_z, \quad (\text{C.4c})$$

$$il\hat{u} + \frac{\partial v}{\partial y} + im\hat{w} = 0, \quad (\text{C.4d})$$

where we have dropped the subscript  $lm$  in the above equation. Next, using the last equation, we eliminate  $\hat{u}$ ,  $\hat{v}$  and  $\hat{w}$  in the first three equations to obtain the following equation for the pressure:

$$\frac{\partial^2 \hat{p}}{\partial^2 y} - k^2 \hat{p} = il\hat{f}_x + \frac{\partial \hat{f}_y}{\partial y} + im\hat{f}_z. \quad (\text{C.5})$$

The continuity equation can be replaced by the above equation for pressure along with the boundary condition requiring the velocity to be divergence free [10, 7], i.e.

$$il\hat{u} + \frac{\partial \hat{v}}{\partial y} + im\hat{w} = 0 \text{ at } y = 0 \quad \& \quad y = H. \quad (\text{C.6})$$

Alternatively, one solves the Eq. C.5 with the following pressure boundary condition

$$\hat{p} = \hat{p}_1 \text{ at } y = 0, \quad (\text{C.7a})$$

$$\hat{p} = \hat{p}_2 \text{ at } y = H, \quad (\text{C.7b})$$

though, the pressure boundary conditions above are unknown a priori, but instead they must take a value so that the condition in Eq. (C.6) is satisfied. Grouping all the equations to be solved, we have the following

$$\frac{\partial^2 \hat{p}}{\partial^2 y} - k^2 \hat{p} = il \hat{f}_x + \frac{\partial \hat{f}_y}{\partial y} + im \hat{f}_z, \quad (\text{C.8a})$$

$$\mu \frac{\partial^2 \hat{u}}{\partial^2 y} - \mu k^2 \hat{u} - il \hat{p} = \hat{f}_x, \quad (\text{C.8b})$$

$$\mu \frac{\partial^2 \hat{v}}{\partial^2 y} - \mu k^2 \hat{v} - \frac{\partial \hat{p}}{\partial y} = \hat{f}_y, \quad (\text{C.8c})$$

$$\mu \frac{\partial^2 \hat{w}}{\partial^2 y} - \mu k^2 \hat{w} - im \hat{p} = \hat{f}_z, \quad (\text{C.8d})$$

with the following boundary conditions

$$\begin{aligned} \hat{p} = \hat{p}_1, \hat{u} = \hat{g}_{1x}, \hat{v} = \hat{g}_{1y}, \hat{w} = \hat{g}_{1z} \text{ at } y = 0, \\ \hat{p} = \hat{p}_2, \hat{u} = \hat{g}_{2x}, \hat{v} = \hat{g}_{2y}, \hat{w} = \hat{g}_{2z} \text{ at } y = H, \end{aligned} \quad (\text{C.9})$$

where  $\mathbf{g}_1 = (g_{1x}, g_{1y}, g_{1z})$  and  $\mathbf{g}_2 = (g_{2x}, g_{2y}, g_{2z})$  and, as with the other quantities,  $\hat{\cdot}$  denotes discrete Fourier transform in  $x$  and  $z$ .

The Kleiser-Schumann influence matrix approach involves solving three set of equations as in Eq. (C.8) with different boundary conditions as discussed shortly. In the first set, one solves the equations in C.8 with the correct boundary conditions for the velocity in Eq. (C.9), but with homogeneous boundary conditions for the pressure, i.e.

$$\hat{p} = 0 \text{ at } y = 0 \ \& \ y = H \quad (\text{C.10})$$

Each of the equations for pressure and velocity components above are solved here by expanding them in discrete Chebyshev polynomials and then employing the Galerkin method to obtain equations for each of Chebyshev modes. The appropriate boundary conditions are satisfied by employing the tau method [6, 49] in which the equations for the highest two Chebyshev modes are replaced by the boundary condition equations. The solution for pressure is first computed, whose value is then substituted in the equations for velocity. Thus, in each step, one needs to solve a Helmholtz equation using Chebyshev polynomial expansion. In this case, the equations for the unknown Chebyshev coefficients can be reduced to a quasi-tridiagonal matrix equation with the last full row being full, while the rest being in the standard tridiagonal form. Also, note that the equations for the even and odd Chebyshev modes are decoupled and solved separately. These quasi-tridiagonal systems of equations can be solved in  $O(N_y)$  time with a direct algorithm [49]. Also, the

use of Chebyshev Gauss-Lobatto quadrature points [6, 49] for transforming a variable between physical and transform space ensures that FFTs can be employed for its evaluation [7]. Therefore, for each of the Fourier modes  $(l, m)$ , the asymptotic cost of the Chebyshev-tau solution procedure scales as  $N_y \log N_y$ . We denote this first set of solution thus obtained for Fourier mode  $(l, m)$  by  $(\hat{u}_a, \hat{v}_a, \hat{w}_a, \hat{p}_a)$ .

The next two sets of equations involve solving the homogeneous version of the differential equations in C.8, i.e., the right hand side of the each of the equations in C.8 is set to zero. Moreover, the velocity boundary condition for these two sets of problems are also homogeneous. The only non-homogeneous equation in these two problems are the pressure boundary conditions. In the first of these, the pressure boundary condition is the following:

$$\hat{p}(0) = 1 \quad \& \quad \hat{p}(H) = 0, \quad (\text{C.11})$$

while in the second the pressure boundary condition is

$$\hat{p}(0) = 0 \quad \& \quad \hat{p}(H) = 1. \quad (\text{C.12})$$

We denote these two solutions by  $(\hat{u}_b, \hat{v}_b, \hat{w}_b, \hat{p}_b)$ , and  $(\hat{u}_c, \hat{v}_c, \hat{w}_c, \hat{p}_c)$ . It is important to note that the latter two set of equations are to be solved just once at the beginning of the simulation and the results are stored. The overall solution for the velocity and pressure is then obtained as:

$$\begin{aligned} \hat{u} &= \hat{u}_a + \hat{p}_1 \hat{u}_b + \hat{p}_2 \hat{u}_c, \\ \hat{v} &= \hat{v}_a + \hat{p}_1 \hat{v}_b + \hat{p}_2 \hat{v}_c, \\ \hat{w} &= \hat{w}_a + \hat{p}_1 \hat{w}_b + \hat{p}_2 \hat{w}_c, \\ \hat{p} &= \hat{p}_a + \hat{p}_1 \hat{p}_b + \hat{p}_2 \hat{p}_c. \end{aligned} \quad (\text{C.13})$$

It is easy to see that the above solution satisfies both the differential equations as well as the boundary conditions. The only remaining task is therefore to determine the pressure boundary conditions  $\hat{p}_1$  and  $\hat{p}_2$ . This is accomplished by the requiring that the velocity be divergence free at the boundary (Eq. C.6). Thus, one obtains the following equations for the pressure boundary conditions

$$\begin{pmatrix} C_b(0) & C_c(0) \\ C_b(H) & C_c(H) \end{pmatrix} \begin{pmatrix} \hat{p}_1 \\ \hat{p}_2 \end{pmatrix} = - \begin{pmatrix} C_a(0) \\ C_a(H) \end{pmatrix} \quad (\text{C.14})$$

In the above equations,  $C_a$ ,  $C_b$  and  $C_c$  are the continuity expression (Eq. C.6) evaluated at the appropriate boundary point, i.e. at  $y = 0$  or  $y = H$ . For example,  $C_a(0)$  is given by

$$C_a(0) = il\hat{u}_a(0) + \frac{\partial \hat{v}_a}{\partial y}(0) + im\hat{w}_a(0) \quad (\text{C.15})$$

The  $2 \times 2$  coefficient matrix in Eq. (C.14) is known as the influence matrix and the resulting matrix equation is trivially solved at a cost of  $O(1)$ . The solution in Eq. (C.13) gives the Fourier coefficients of the pressure

and velocity as a function of the wall normal coordinate  $y$ , which is then employed to obtain the pressure and velocity in the physical space using inverse FFTs.

## References

- [1] Allen, M. P., Tildesley, D. J., 1989. *Computer Simulation of Liquids*. Oxford University Press.
- [2] Bagchi, P., Kalluri, R. M., 2010. Rheology of a dilute suspension of liquid-filled elastic capsules. *Physical Review E* 81, 056320.
- [3] Barthes-Biesel, D., 2011. Modeling the motion of capsules in flow. *Current Opinion in Colloid & Interface Science*. 16, 3–12.
- [4] Barthes-Biesel, D., Diaz, A., Dhenin, E., 2002. Effect of constitutive laws for two-dimensional membranes on flow-induced capsule deformation. *Journal Of Fluid Mechanics* 460, 211–222.
- [5] Blake, J. R., 1971. A note on the image system for a stokeslet in a no-slip boundary. *Proceedings of the Cambridge Philosophical Society* 70, 303–310.
- [6] Canuto, C., Hussaini, M. Y., Quarteroni, A., Zang, T. A., 2006. *Spectral Methods Fundamentals in Single Domain*. Springer-Verlag.
- [7] Canuto, C., Hussaini, M. Y., Quarteroni, A., Zang, T. A., 2007. *Spectral Methods Evolution to Complex Geometries and Applications to Fluid Dynamics*. Springer-Verlag.
- [8] Charrier, J. M., Shrivastava, S., Wu, R., 1989. Free and constrained inflation of elastic membranes in relation to thermoforming - non-axisymmetric problems. *Journal Of Strain Analysis For Engineering Design* 24, 55–74.
- [9] Deserno, M., Holm, C., 1998. How to mesh up ewald sums. i. a theoretical and numerical comparison of various particle mesh routines. *Journal of Chemical Physics* 109, 7678–7693.
- [10] Deville, M., Kleiser, L., Montigny-Rannou, F., 1984. Pressure and time treatment for chebyshev spectral solution of a stokes problem. *International Journal for Numerical Methods in Fluids* 4, 1149–1163.
- [11] Doddi, S. K., Bagchi, P., 2009. Three-dimensional computational modeling of multiple deformable cells flowing in microvessels. *Physical Review E* 79, 046318.
- [12] Elman, H. C., Silvester, D. J., Wathen, A. J., 2005. *Finite elements and fast iterative solvers: with applications in incompressible fluid dynamics*. Oxford University Press.
- [13] Fard, A. S., Hulsen, M., Meijer, H., Famili, N., Anderson, P., 2012. Adaptive non-conformal mesh refinement and extended finite element method for viscous flow inside complex moving geometries. *International Journal for Numerical Methods in Fluids* 68 (8), 1031–1052.
- [14] Ferziger, J. H., Peric, M., 2002. *Computational methods for fluid dynamics*. Springer-Verlag.
- [15] Foss, D. R., Brady, J. F., 2000. Brownian Dynamics simulation of hard-sphere colloidal dispersions. *Journal of Rheology* 44, 629–651.
- [16] Freund, J. B., 2007. Leukocyte margination in a model microvessel. *Physics of Fluids* 19, 023301.
- [17] Fung, Y. C., 1996. *Biomechanics: Circulation*, 2nd Edition. Springer-Verlag.
- [18] Greengard, L., Kropinski, M. C., Mayo, A., 1996. Integral equation methods for stokes flow and isotropic elasticity in the plane. *Journal of Computational Physics* 125, 403–414.
- [19] Greengard, L., Lee, J.-Y., 2004. Accelerating the nonuniform fast fourier transform. *SIAM Review* 46, 443–454.
- [20] Greengard, L., Rokhlin, V., 1987. A fast algorithm for particle simulations. *Journal of Computational Physics* 73, 325–348.
- [21] Griggs, A. J., Zinchenko, A. Z., Davis, R. H., 2007. Low-Reynolds-number motion of a deformable drop between two parallel plane walls. *International Journal of Multiphase Flow* 33, 182–206.
- [22] Hasimoto, H., 1959. On the periodic fundamental solutions of the Stokes equations and their application to viscous flow past a cubic array of spheres. *Journal of Fluid Mechanics* 5, 317–328.
- [23] Henniger, R., Obrist, D., Kleiser, L., 2010. High-order accurate solution of the incompressible Navier-Stokes equations on massively parallel computers. *Journal of Computational Physics* 229, 3543–3572.
- [24] Hernandez-Ortiz, J. P., de Pablo, J. J., Graham, M. D., 2007. Fast computation of many-particle hydrodynamic and electrostatic interactions in a confined geometry. *Physical Review Letters* 98, 140602.
- [25] Hernandez-Ortiz, J. P., Ma, H., de Pablo, J. J., Graham, M. D., 2008. Concentration distributions during flow of confined flowing polymer solutions at finite concentration: slit and grooved channel. *Korea-Australia Rheology Journal* 20, 143–152.
- [26] Hughes, T. J. R., 1987. *The Finite element method : linear static and dynamic finite element analysis*. Prentice-Hall.
- [27] Janssen, P. J. A., Anderson, P. D., 2007. Boundary-integral method for drop deformation between parallel plates. *Physics of Fluids* 19, 043602.
- [28] Janssen, P. J. A., Anderson, P. D., 2008. A boundary-integral model for drop deformation between two parallel plates with non-unit viscosity ratio drops. *Journal of Computational Physics* 227, 8807–8819.
- [29] Kennedy, M. R., Pozrikidis, C., Skalak, R., 1994. Motion and deformation of liquid drops, and the rheology of dilute emulsions in simple shear flow. *Computers & Fluids* 23, 251–278.
- [30] Kim, S., Karrila, S. J., 2005. *Microhydrodynamics: Principles and Selected Applications*. Dover Publications.
- [31] Kumar, A., Graham, M. D., 2011. Segregation by membrane rigidity in flowing binary suspensions of elastic capsules. *Physical Review E* 84, 066316.
- [32] Kumar, A., Higdon, J. J. L., 2010. Origins of the anomalous stress behavior in charged colloidal suspensions under shear. *Physical Review E* 82, 051401.
- [33] Kumar, A., Higdon, J. J. L., 2011. Dynamics of the orientation behavior and its connection with rheology in sheared non-brownian suspensions of anisotropic dicolloidal particles. *Journal of Rheology* 55, 581–626.
- [34] Kumar, A., Higdon, J. J. L., 2011. Particle mesh ewald stokesian dynamics simulations for suspensions of non-spherical particles. *Journal of Fluid Mechanics* 675, 297–335.
- [35] Lac, E., Barthes-Biesel, D., Pelekasis, N. A., Tsamopoulos, J., 2004. Spherical capsules in three-dimensional unbounded Stokes flows: effect of the membrane constitutive law and onset of buckling. *Journal of Fluid Mechanics* 516, 303–334.

- [36] Lac, E., Morel, A., Barthès-Biesel, D., 2007. Hydrodynamic interaction between two identical capsules in simple shear flow. *Journal of Fluid Mechanics* 573, 149–169.
- [37] Lambert, J. D., 1997. *Numerical Methods for Ordinary Differential Systems: The Initial Value Problem*. John Wiley & Sons Ltd.
- [38] Le, D.-V., Tan, Z., 2010. Large deformation of liquid capsules enclosed by thin shells immersed in the fluid. *Journal of Computational Physics* 229, 4097–4116.
- [39] Li, X., Sarkar, K., 2008. Front tracking simulation of deformation and buckling instability of a liquid capsule enclosed by an elastic membrane. *Journal of Computational Physics* 227, 4998–5018.
- [40] Lindbo, D., Tornberg, A.-K., 2010. Spectrally accurate fast summation for periodic stokes potentials. *Journal of Computational Physics* 229, 8994–9010.
- [41] Lindbo, D., Tornberg, A.-K., 2011. Spectral accuracy in fast ewald-based methods for particle simulations. *Journal of Computational Physics* 230, 8744–8761.
- [42] Liron, N., Mochon, S., 1976. Stokes flow for a stokeslet between two parallel flat plates. *Journal of Engineering Mathematics* 10, 287–303.
- [43] Loewenberg, M., Hinch, E. J., 1996. Numerical simulation of a concentrated emulsion in shear flow. *Journal of Fluid Mechanics* 321, 395–419.
- [44] MacMeccan, R. M., Clausen, J. R., Neitzel, G. P., Aidun, C. K., 2009. Simulating deformable particle suspensions using a coupled lattice-Boltzmann and finite-element method. *Journal of Fluid Mechanics* 618, 13–39.
- [45] Meng, Q., Higdon, J. J. L., 2008. Large scale dynamic simulation of plate-like particle suspensions. part ii: Brownian simulation. *Journal of Rheology* 52, 37–65.
- [46] Metsi, E., 2000. Large scale simulation of bidisperse emulsions and foams. Ph.D. thesis, University of Illinois at Urbana-Champaign.
- [47] Muldowney, G., Higdon, J. J. L., 1995. A spectral boundary element approach to three-dimensional Stokes flow. *Journal of Fluid Mechanics* 298, 167–192.
- [48] Noguchi, H., Gompper, G., 2005. Shape transitions of fluid vesicles and red blood cells in capillary flows. *Proceedings of the National Academy of Sciences, USA* 102, 14159–14164.
- [49] Peyret, R., 2002. *Spectral Methods for Incompressible Viscous Flow*. Springer-Verlag.
- [50] Pozrikidis, C., 1992. *Boundary Integral and Singularity Methods for Linearized Viscous Flow*. Cambridge University Press.
- [51] Pranay, P., Anekal, S. G., Hernandez-Ortiz, J. P., Graham, M. D., 2010. Pair collisions of fluid-filled elastic capsules in shear flow: effects of membrane properties and polymer additives. *Physics of Fluids* 22, 123103.
- [52] Rahimian, A., Veerapaneni, S. K., Biros, G., 2010. Dynamic simulation of locally inextensible vesicles suspended in an arbitrary two-dimensional domain, a boundary integral method. *Journal of Computational Physics* 229, 6466–6484.
- [53] Rallison, J. M., 1981. A numerical study of the deformation and burst of a viscous drop in general shear flows. *Journal of Fluid Mechanics* 109, 465–482.
- [54] Ramanujan, S., Pozrikidis, C., 1998. Deformation of liquid capsules enclosed by elastic membranes in simple shear flow: large deformations and the effect of fluid viscosities. *Journal of Fluid Mechanics* 361, 117–143.
- [55] Saad, Y., 2003. *Iterative Methods for Sparse Linear Systems*. Society for Industrial and Applied Mathematics.
- [56] Silvester, D. J., Wathen, A. J., 1994. Fast iterative solution of stabilised Stokes systems part ii: Using general block preconditioners. *SIAM Journal on Numerical Analysis* 31, 1352–1367.
- [57] Smart, J. R., Leighton, D. T., 1991. Measurement of the drift of a droplet due to the presence of a plane. *Physics of Fluids A* 3, 21–28.
- [58] Staben, M. E., Zinchenko, A. Z., Davis, R. H., 2003. Motion of a particle between two parallel plane walls in low-reynolds-number Poiseuille flow. *Physics of Fluids* 15, 1711–1733.
- [59] Stone, H. A., Stroock, A. D., Ajdari, A., 2004. Engineering flows in small devices: Microfluidics toward a lab-on-a-chip. *Annual Review of Fluid Mechanics* 36, 381–411.
- [60] Swan, J. W., Brady, J. F., 2011. The hydrodynamics of confined dispersions. *Journal of Fluid Mechanics* 687, 254–299.
- [61] Thibault, J. C., Senocak, I., 2009. Cuda implementation of a Navier-Stokes solver on multi-gpu desktop platforms for incompressible flows. In: 47th AIAA Aerospace Sciences Meeting.
- [62] Veerapaneni, S. K., Rahimian, A., Biros, G., Zorin, D., 2011. A fast algorithm for simulating vesicle flows in three dimensions. *Journal of Computational Physics* 230, 5610–5634.
- [63] Zhao, H., Isfahani, A. H. G., Olson, L. N., Freund, J. B., 2010. A spectral boundary integral method for flowing blood cells. *Journal of Computational Physics* 229, 3726–3744.
- [64] Zinchenko, A. Z., Davis, R. H., 2000. An efficient algorithm for hydrodynamical interaction of many deformable drops. *Journal of Computational Physics* 157, 539–587.
- [65] Zinchenko, A. Z., Davis, R. H., 2002. Shear flow of highly concentrated emulsions of deformable drops by numerical simulations. *Journal of Fluid Mechanics* 455, 21–62.